Morris, J.D., Villinger, H.W., Klaus, A., et al., 2003
Proceedings of the Ocean Drilling Program, Initial Reports Volume 205

6. Site 1255[1]

Shipboard Scientific Party[2]

SITE SUMMARY

Site 1255 is located ~0.4 km arcward from the deformation front at a water depth of 4311.6 m and in close vicinity to the holes of Site 1043 drilled during Leg 170 (Kimura, Silver, Blum, et al., 1997). Hole 1255A is ~20 m east of Hole 1043A and ~30 m northwest of Hole 1043B (Figs. **F1, F2, F3**). In Hole 1043A the complete section was cored to 282 meters below seafloor (mbsf) in the underthrust sequence (Unit U3), whereas Hole 1043B was logged using logging while drilling (LWD) to 482 mbsf, the top of the igneous basement. As both holes penetrated the décollement, their results were used to plan the drilling strategy and the installation of the CORK-II observatory.

The objective of Site 1255 was to identify the décollement with "real-time" geochemical analyses and penetration rate and to install a long-term observatory for monitoring of fluid flow, pressure, and temperature in the décollement. Because of time constraints, only four cores were taken from 123 to 157 mbsf. We recovered 7.2 m (21%) from the 34-m cored section. Because of the limited recovery and whole-round sections taken for pore water analyses for locating the décollement, other studies on the cores were limited.

The seismic record (Fig. **F3**) in the vicinity of Hole 1255A (common midpoint 3174) shows no coherent reflections above the décollement. This reflects the general chaotic sedimentary pattern observed already in cores from Site 1254 and in Leg 170 results. The confused seafloor reflection pattern, masking a clear seafloor identification, is probably due to side echoes, generated by local bathymetric relief (Fig. **F1**). The first prominent reflector relevant for drilling is at 5.96 s two-way traveltime, which marks the boundary between margin sediments and the underthrust sequence, cored at 144 mbsf in Hole 1255A. The current seismic data do not show any evidence for fault zones above the décollement.

F1. Bathymetric map of Leg 205 and 170 drill sites, p. 22.

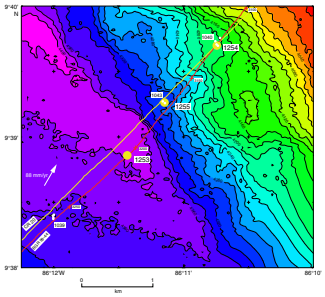

F2. Location of Site 1255, p. 23.

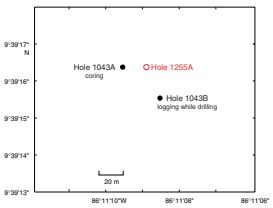

F3. Multichannel seismic profile BGR 99-44, p. 24.

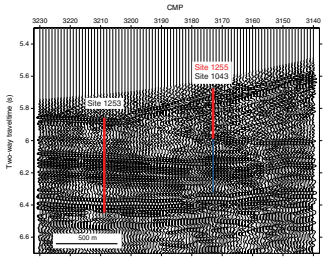

[1]**Examples of how to reference the whole or part of this volume.**
[2]**Shipboard Scientific Party addresses.**

Ms 205IR-106

After setting the reentry cone in Hole 1255A, we drilled to a depth of 123 mbsf with a 14¾-in bit. We then installed 10¾-in casing to a depth of 117 mbsf and cemented it in. Coring started at 123 mbsf, after drilling out the cement shoe, and stopped at 157 mbsf when a sudden increase in penetration rate during cutting of the fourth core indicated that the underthrust sediments were reached. The installation of the CORK-II was successful and completed with the deployment of the remotely operated vehicle (ROV) platform. A postcruise *Alvin* dive showed the installation to be fully operational, and pressure data showed a return to hydrostatic conditions within the borehole.

Lithostratigraphy

The section recovered from Hole 1255A can be separated into lithostratigraphic Unit T1 (equivalent to Subunit P1B at Site 1254) and Subunit U1A just beneath the level of the décollement at 144.08 mbsf. The division marks a sharp junction between a series of structureless greenish gray claystones with silts and few or no diatoms above an underlying series of diatom-rich claystones with interbedded silts, sands, and occasional fine-grained conglomerates. The clastic sediments in the underthrust section (Subunit U1A), interpreted as near-trench turbidites during Leg 170, differ from the purely hemipelagic diatom ooze recovered at Site 1043 (Kimura, Silver, Blum, et al., 1997). The fact that these turbidites were not recovered at Site 1043 may indicate that this section is very thin and simply not recovered or not present at all because of lateral facies changes over short distances. Blocks of reworked carbonate in Unit T1 indicate that these sediments are mostly debris flow deposits, in part derived originally from shallow nearshore environments. The presence of a pelagic nannofossil chalk interval and the larger proportion of diatoms at Site 1255 suggests that this site experienced a larger amount of pelagic sedimentation than did Site 1254. The underthrust section represents a trench depositional setting, with turbidite silts and sands interbedded with hemipelagic mudstones. Unlike other sites cored during Leg 205, sediments at Site 1255 contain no primary ash layers in the short section recovered; however, fresh and altered volcanic glass shards do compose a significant proportion (10%–15%) of the prism sediments.

Structural Geology

At Site 1255, structural deformation, with brecciation and polished clast surfaces as an indication of incipient scaly fabric, increases within the recovered section from 132.7 mbsf to the base of the décollement at 144.08 mbsf. The top of the décollement zone could not be defined as a result of limited coring and recovery. The base of the décollement is sharp and well defined and coincides with the division between Unit T1 and Subunit U1A. Only one measurement of bedding dip (44°) was possible in the décollement zone. The hemipelagic layers in the underthrust section below 144.08 mbsf show some medium-scale brecciation (1- to 3-cm fragments) with unpolished surfaces, whereas the sandy layers are undeformed.

Organic Geochemistry

Volatile hydrocarbon gases were sampled using the vacutainer and headspace technique. As no gas voids were apparent at Site 1255, in

contrast to Site 1254, vacutainer samples show large air contamination. Headspace CH_4 concentrations drop rapidly from >3000 ppmv in Core 205-1255A-2R to 5 ppmv below the décollement (145 mbsf). Propane, as an indicator for deeply sourced fluids, is low in the prism section (~1 ppmv) and absent below the décollement.

Inorganic Geochemistry

Only three whole rounds (one per core) could be taken for geochemical analyses of pore waters because of low recovery, and all conclusions are therefore somewhat speculative. As observed at Site 1254, the chemical composition of the pore fluids at Site 1255 also is distinctly different in the wedge and underthrust section, with a less sharp transition at the base of the décollement zone at ~144 mbsf. Fluid flow is indicated by salinity, Na and Ca concentration minima, and a Li concentration maximum within the décollement sample at 134.2 mbsf. Similar concentration variations were observed at Site 1043 along with a magnesium concentration maximum within the same interval. Across the décollement, changes in Ca and Mg concentrations are in the opposite direction to those seen at Site 1254. In general, the pore fluids within the upper fault zone and in the décollement at Sites 1254 and 1040 are characterized by having a significantly stronger signature of a deeply sourced fluid than the pore fluids from Sites 1255 and 1043 (see **"Inorganic Geochemistry,"** p. 27, in the "Site 1254" chapter). At Sites 1255 and 1043, the pore fluid chemistry in the wedge and the uppermost underthrust sediments appears to reflect some mixing between the lower wedge and uppermost hemipelagic pore fluids, thereby partially obscuring the deeply sourced fluid signature observed at Site 1254. This pore water mixing could be achieved by advection of fluid from the underthrust section across the décollement and into the lower wedge.

Microbiology

Two samples for microbiological investigations were taken and either frozen or fixed for postcruise adenosine-triphosphate (ATP) quantification, deoxyribonucleic acid (DNA) assessment, or cell counts. Samples of drilling water were frozen as well to evaluate contamination of cores. The chemical tracer for quantifying microbiological contamination was not deployed during coring in Hole 1255A because of concern that the trace element chemistry of the perfluorocarbon tracer may affect postcruise pore fluid geochemical analyses. Particulate tracer tests yielded fluorescent microsphere counts suggesting very low to no particulate contamination in the interior of the microbiology whole rounds.

Paleomagnetism

Paleomagnetic declination and inclination, measured on discrete samples and archive halves, disagree only in the upper part (132.76–134.84 mbsf) of the cored interval, making any magnetostratigraphic interpretation questionable within this interval. Across the décollement, a clear polarity change can be seen in both archive halves and discrete samples. However, the polarity changes cannot be assigned to a particular chron and are not usable for dating purposes. Magnetic intensities and susceptibilities are generally low in the upper part of the section but increase substantially in the sandy layers of the underthrust sequence.

Physical Properties

Sample porosities and LWD porosities from Leg 170 show a clear increase at the base of the décollement from values of ~55% in the prism section to values of ~70% in the underthrust. Sample porosities from Hole 1255A clearly confirm the values in the prism, but the few data points below the décollement are not representative of the porosity of the underthrust sequence but, rather, show the influence of sampling clayey or sandy material. Only the magnetic susceptibility shows a marked increase below the décollement, which reflects a presumably higher magnetite content in the turbidites of the underthrust.

CORK-II Installation

A CORK-II observatory was successfully installed as shown in Figure **F4.** The center of the packer is at 129 mbsf and the center of the screen at 140 mbsf, in the middle of the geochemical anomaly as determined from Site 1255 data and Site 1043 results. The second pressure port inside a small screen was installed just above the upper packer. This CORK-II installation was also visited by the *Alvin* shortly after Leg 205 and was found to be fully operational (see **"Postcruise *Alvin* Submersible Visit to Site 1253 and 1255 CORK-IIs,"** p. 36, in the "Leg 205 Summary" chapter.).

F4. Hole 1255A borehole installation, p. 25.

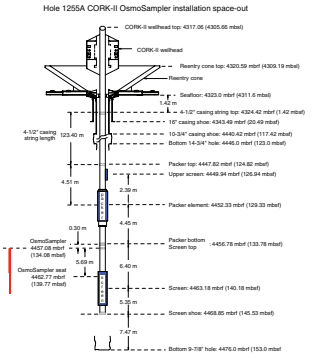

OPERATIONS

Site 1255 (Proposed Site 1043R)

The beacon at Site 1254 was released at 1106 hr and was on deck at 1221 hr on 26 October 2002 (all times reported are local ship time, which is Universal Time Coordinated – 5 hr). The ship moved the ~1.1 nmi to Site 1255 in dynamic-positioning mode while the CORK-II wellhead was being recovered. We deployed a seafloor position beacon at Site 1255 at 2116 hr on 26 October.

A reentry cone was then moved onto the moonpool doors and two joints (20 m) of 16-in casing were assembled to a 16-in casing hanger and latched into the reentry cone. A jetting bottom-hole assembly (BHA) was assembled and latched into the 16-in casing hanger. At 2000 hr on 26 October, the reentry cone was lowered to the seafloor. Because of the complex seafloor topography in the vicinity of the drill site, the 3.5-kHz precision depth recorder returned six different echoes. The most conservative shallowest depth indicated (4234 meters below rig floor [mbrf]) was used. The casing was lowered to 4325 mbrf before the seafloor was detected by a reduction in drill string weight. Hole 1255A was started at 0550 hr on 27 October when jetting-in of the 16-in casing began.

The 16-in casing was jetted in to 4343.49 mbrf (20.49 mbsf) in 5 hr. The casing running tool was released, pulled out of the hole, and was back on the rig floor at 2045 hr on 27 October. The next step was to prepare the hole for installing 10¾-in casing. A BHA with a 14¾-in drilling bit was assembled and lowered to the seafloor, and Hole 1255A was reentered at 0430 hr on 28 October. We drilled from 4343.49 to 4446 mbrf (20.49 to 123 mbsf). The hole was swept with 50 barrels of sepiolite, and then the complete borehole volume was circulated with seawater. We then conducted a wiper trip by raising the bit to the 16-in

casing shoe at 4343.49 mbrf (20.49 mbsf) and then lowering it back down to 4429 mbrf (106 mbsf), where slight weight was taken. The hole was washed and reamed from 4429 mbrf (106 mbsf) back to total depth (4446 mbrf; 123 mbsf). The hole was again swept with 50 barrels of sepiolite, twice the hole volume was circulated with seawater, and 85 barrels of sepiolite was pumped into the hole in preparation for deploying 10¾-in casing. The bit was then pulled out of the hole and was back on the rig floor at 0526 hr on 30 October.

Ten joints of 10¾-in casing (115.5 m) were made up with a 10¾-in Dril-Quip casing hanger. A casing cementing plug was then made up to the Dril-Quip casing running tool that, in turn, was latched into the casing hanger. The 10¾-in casing string was then lowered to the seafloor. Hole 1255A was reentered with the casing at 1629 hr on 29 October. The casing was lowered to 4425 mbrf (102 mbsf) when slight resistance was encountered. The top drive was picked up and the casing was washed in to a total depth of 117.42 mbsf. After the casing hanger was confirmed to be latched into the reentry cone (10,000 lb overpull), the casing was cemented in place with 20 barrels of 15.8-lb/gal cement.

The casing running tool was released at 1940 hr on 29 October and pulled clear of the reentry cone. Before the drill string was tripped back to the ship, the drill line had to be slipped and cut. The casing running tool was back on deck at 0405 hr on 30 October.

A rotary core barrel (RCB) BHA was assembled and lowered to the seafloor, and Hole 1255A was reentered at 1207 hr on 30 October. It took 4.5 hr to drill out the 10¾-in casing shoe with the RCB bit before coring began.

We then cut four RCB cores (Cores 205-1255A-1R through 4R) (Table T1) from 4446.0 to 4480.0 mbrf (132.7 to 157.0 mbsf) and recovered 7.22 m (21%). Once the base of the décollement was identified (based on a substantial change in penetration rate), we began preparing the hole for installing the CORK-II and OsmoSampler.

T1. Coring summary for Site 1255, p. 44.

We swept the hole with 50 barrels of sepiolite, and the borehole volume was circulated with seawater. The bit was raised up to the 10¾-in casing shoe and then lowered back down to 4467 mbrf (144 mbsf), where the bit took weight; the hole was reamed and washed from there to 4476.0 mbrf (153.0 mbsf). Once again, we swept the hole clean with 50 barrels of sepiolite and then circulated the borehole volume with seawater. The bit was again raised up to the 10¾-in casing shoe and then lowered back down to total depth with only slight drag near the bottom of the hole. To keep the hole open without exposing the décollement to barite-weighted mud, 20 barrels of sepiolite was placed in the bottom of the hole. The bit was pulled up to 4416 mbrf (93 mbsf) inside the 10¾-in casing, and the hole was displaced with 32 barrels of heavy mud. The bit was pulled out of the hole and was back on the rig floor at 2015 hr on 31 October.

A CORK-II consisting of a screen, packer, 123.4 m of 4½-in casing, and a CORK-II wellhead was assembled. The CORK-II assembly was lowered to the seafloor to just above the reentry cone. The top drive was picked up so we could pump seawater through the end of the 4½-in casing as it was lowered in the hole to displace the heavy mud and keep the screen clean. Hole 1255A was reentered at 1000 hr on 1 November, and the 4½-in casing was lowered to 4465 mbrf (142 mbsf) while seawater was circulated.

The OsmoSampler seat was attached to the coring wireline and lowered down the drill string. The seat landed and was jarred on to latch the lock mandrel in place. When the wireline was recovered, the seat

was still attached and the running tool was partially sheared and the seat seals were missing. The running tool was redressed, new seals were installed on the seat, and the seat was lowered back down the drill string. The seat landed in what appeared to be the upper latch nipple at top of the packer. The mud pump was engaged, the drill string was pressured to 300 psi, and the seat passed through the upper latch nipple. The seat was then lowered until it landed in the middle latch nipple at the top of the screen. Once again the pump was engaged, and the seat passed through the middle latch nipple. The seat was then lowered until it landed in the latch nipple inside the screen. The pump was engaged to fully latch the seat. The seat was jarred down on to latch the lock mandrel in place. An overpull of 3000 lb was applied and held, indicating that the lock mandrel was latched in place. The running tool was then jarred up on and released. The running tool was then pulled out of the hole and redressed.

When the OsmoSampler was attached to the running tool on the rig floor, the screws holding the OsmoSampler top connection in place were sheared. The running tool was removed, and the broken OsmoSampler was replaced with another one. The OsmoSampler fill port pipe plug (inside the top connection of the OsmoSampler) was protruding above the bottom of the blind box, preventing the double pin crossover sub to be properly attached. Bakerlok was applied to the double pin sub, and the sub was made up to the OsmoSampler top connection. Bakerlok was also applied to the collet housing, and the housing was made up to the OsmoSampler probe tip.

The OsmoSampler assembly picked up with a tugger and landed in the top of the drill pipe. The coring wireline was attached to the assembly, and it was lowered down the drill string in stages to allow pressure equalization of the osmotic pumps. Because the OsmoSampler lock mandrel had no seals, it easily passed through the upper latch nipple and was landed on top of the seat.

With the OsmoSampler probe tip stung through the seat, all of the OsmoSampler sampling ports were sealed off from the 4½-in casing above. The pump was engaged to fully seat the OsmoSampler and help hold the assembly down during jarring. The running tool was jarred in order to latch the lock mandrel in place. When the wireline was raised, no overpull was observed and the weight of the OsmoSampler was lost, indicating that the running tool had released.

The OsmoSampler seat allows the pressure below and above the ported seal bore and plug to equalize. Thus, when the OsmoSampler probe tip is stung into the seat, the OsmoSampler is pressure balanced, so confirmation of latch-in (requiring pulling the OsmoSampler and deploying it again) was not critical to the installation. Once we verified that the OsmoSampler was at the correct depth (by tagging it with the wireline), we pulled the running tool out of the hole.

The modified packer setting go-devil was then dropped down the drill string and chased with the coring wireline without latch. The go-devil was tagged inside the CORK-II running tool, and the wireline was pulled out of the hole.

The CORK-II wellhead was then landed and latched into the reentry cone at 2000 hr on 1 November. The drill string was pressurized to 1200 psi for 30 min to inflate the packer. The drill string pressure was then increased to 1800 psi for 10 min to shift the spool valves. While the packer was set, the vibration-isolated television (VIT) camera system was pulled out of the hole in preparation for deploying the ROV platform.

The ROV platform was assembled around the drill string in the moonpool. The deployment bridle and the logging line were then attached. The platform was lowered down the drill string on the logging line and landed on the reentry cone.

At 0155 hr on 2 November, the acoustic releases were activated. When the logging line was picked up, overpull was observed, suggesting that the ROV platform was not completely free. The logging line was lowered and the acoustic releases were activated again. When the logging line was picked up, overpull was observed again. The overpull was increased above the weight of the platform, indicating the deployment bridle was hung up on something. The logging line was worked for 30 min without freeing the bridle when a straight pull was applied. The bridle came free with ~4500 lb overpull (9100 lb total wire load) and was pulled out of the hole.

When the bridle was recovered, one of the nylon strap termination eyes was found to have failed. The acoustic release yoke may have hung up in the nylon strap eye and had been pulled down to the platform strap bail. When overpull was applied, the platform was pulled up on one side only until the strap failed. If this scenario is correct, there should be no damage to the wellhead. After recovering the platform deployment bridle, the camera was lowered to inspect the installation and no problems with the installation were observed. The CORK-II running tool was released at 0615 hr on 2 November. The running tool and VIT camera system were then recovered; the running tool was back on the rig floor at 1600 hr on 2 November.

Once the seafloor positioning beacon was released (0759 hr) and back on deck (0929 hr on 2 November), we moved back to Hole 1254B in dynamic-positioning mode to attempt to fish the screen, packer, and 4½-in casing that was left in the hole.

The Site 1255 CORK-II was visited ~1 month following installation. After fully closing one of the sampling valves, the CORK-II was functioning properly. For details of the *Alvin* dive and video for the CORK-II installation see **"Postcruise *Alvin* Submersible Visit to Site 1253 and 1255 CORK-IIs,"** p. 36, in the "Leg 205 Summary" chapter.

LITHOSTRATIGRAPHY

As at other Ocean Drilling Program (ODP) drill sites within the Costa Rica forearc wedge, the sediment recovered at Site 1255 is dominated by fine-grained clastic facies. Dark greenish gray claystones with variable proportions of biogenic pelagic sediments and coarse siltstones and sandstones were recorded. Coring at Site 1255 resampled the interval above and below the décollement seen at Site 1043 (Fig. **F5**) (Shipboard Scientific Party, 1997) and so penetrated the lowermost lithostratigraphic division of the forearc wedge defined as Unit T1 at Site 1043. Unit T1 represents a lateral equivalent of lithostratigraphic Subunit P1B at Sites 1254 and 1040 (see **"Lithostratigraphy,"** p. 13, in the "Site 1254" chapter) but was distinguished as the toe of the forearc wedge on the basis of the slightly different sediment facies (i.e., intervals of clay and silty clay interbedded with thin intervals of matrix-supported breccia) (Shipboard Scientific Party, 1997).

As at Sites 1254 and 1040, the transition from the forearc wedge unit into the underthrust section (Subunit U1A) is best charted by the variability in diatom abundance seen in microscopic smear slide analysis. This is because in the cut core surface the two units both appear to be

F5. Stratigraphic log, Site 1255, p. 26.

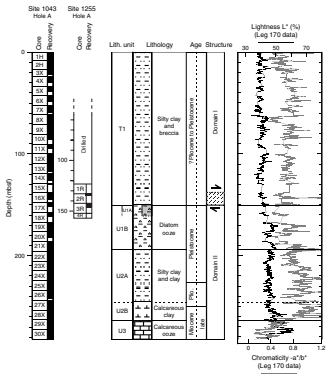

dominated by structureless greenish gray claystones with minor variations in the proportion of clay that cause slight changes in color (Fig. F6). Certainly the color scanner data show no strong shift in either lightness or chromaticity downsection across the décollement (Fig. F5). Clastic units are noted both above and below the unit boundary, making a ready distinction difficult.

Microscopic analysis shows a downcore increase in the abundance of diatoms (Fig. F7). These represent 1% or less of the total sediment toward the top of Section 205-1255A-2R-1 (132.70 mbsf), then increase to 5%–8% of the total sediment volume in Section 205-1255A-2R-3 (134.42 mbsf) (Fig. F8B), and finally rise to >20% below Section 205-1255A-3R-2, 18 cm (144.08 mbsf; Fig. F9). The full smear slide analyses are presented in **"Site 1255 Smear Slides."**

Figure F8D shows a typical example of the sediment with >20% diatoms from within the underthrust lithostratigraphic Subunit U1A. This sediment contains whole well-preserved diatoms and silicoflagellates, as well as rare radiolarians within the otherwise homogeneous clay-rich sediment. There is a clear transition between largely clastic diatom-free claystone at shallow depths in the forearc wedge through a zone of low (5%–8% in Section 205-1255A-2R-3) diatom concentration into a more diatom-rich hemipelagic sequence below. We choose to place our unit boundary in Section 205-1255A-3R-2, 18 cm (144.08 mbsf), the level below which diatoms are very abundant, following the scheme followed at Site 1043 (Shipboard Scientific Party, 1997). The top of lithostratigraphic Subunit U1A is 144.08 mbsf at Site 1255, compared to 150.57 mbsf in Hole 1043A. We do not consider the difference between these two depths to be significant because the proportion of recovery in each core is rather low. The recovered material in Core 205-1255A-3R is necessarily curated to the top of the drilled interval, whereas in reality it may have been recovered from anywhere within the upper 5.31 m of that interval. Given that the real uncertainty in depth is greater than the apparent mismatch, there is no reason to require a difference in décollement depths between these neighboring sites.

Sand–Silt Intervals

Real differences between Sites 1043 and 1255 are apparent in the sedimentary facies of the underthrust sediments. The sediments under the décollement at Site 1255 are more clastic than the purely hemipelagic diatomaceous oozes found at Site 1043. At the unit boundary itself, the underlying sediments comprise a graded sand unit with a microconglomeratic base. The lower part of Core 205-1255A-3R shows several dark-colored muddy sand/silt units, either normally graded or massive with sharp tops and bases suggestive of a redeposited origin. Of particular note is the presence of a 4-cm-thick conglomerate layer in interval 205-1255A-3R-3, 97–101 cm (146.20 mbsf), with clasts up to 1 cm in diameter suspended in a coarse sand matrix and grading up into a 15-cm-thick sandstone interval overlain in turn by a 1-cm-thick claystone (Fig. F10).

We interpret the sandstone unit as the product of deposition from a turbidity current, likely within the trench axis given the stratigraphic location at the top of the underthrust section. The presence of common glauconite, mica, quartz, and feldspar grains within the sand supports an origin of these sediments by erosion of the Costa Rica arc and redeposition downslope toward the trench. Other redeposited clastic intervals include intervals 205-1255A-3R-3, 35–60 cm (145.58 mbsf), and

F6. Fine-grained sediments with a variable proportion of clay, p. 27.

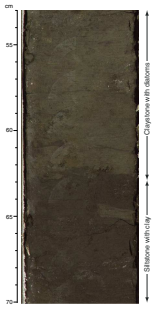

F7. Smear slide data, Sites 1255 and 1043, p. 28.

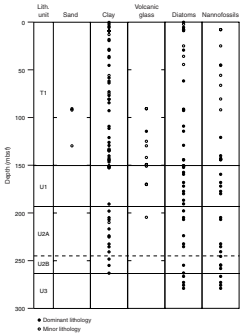

F8. Sediments recovered at Site 1255, p. 29.

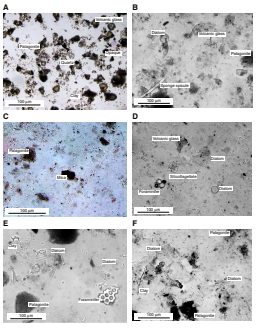

F9. Color contrast between claystone with silt and clay-rich diatom-bearing sediment, p. 30.

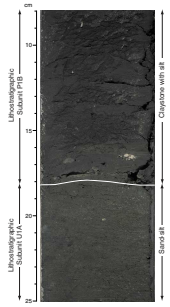

3R-3, 66–84 cm (145.89 mbsf). Because the total thickness recovered below the décollement at Site 1255 is so small (2.3 m), it is not clear how thick these clastic units are. However, the fact that they were not recognized at Site 1043 indicates that this may be a thin interval. Possibly, these sediments were not recovered at Site 1043. Alternatively, they may be tectonically excised by underthrusting at Site 1043 or they may never have accumulated there because of lateral facies changes over short distances in this trench environment. The current data set does not allow a definitive answer to these possibilities. Nonetheless, we define the underthrust section at Site 1255 as lithostratigraphic Subunit U1A, contrasting with the purely hemipelagic Subunit U1B underlying the décollement at Site 1043.

Redeposited Blocks

Further evidence for redeposition in this sequence is seen in interval 205-1255A-3R-1, 144–148 cm (143.84 mbsf), just above the lithostratigraphic unit boundary, where a couple of angular light-colored carbonate blocks are identified (Fig. **F11A**). These blocks are up to 18 mm in diameter and are suspended in a matrix of claystone with silt. Significant recrystallization of the limestone is observed under microscopic analysis (Fig. **F11B**), with needlelike crystals of calcite composing much of the matrix. A minor proportion of the rock is composed of microcrystalline carbonate grains, up to 500 µm in diameter, together with trace amounts of silt-sized altered volcanic material (palagonite). The cobbles may be defined as wackestone fragments. The lithology appears to be exotic to the background sediment and by comparison with similar clasts found in the overthrust forearc wedge sequences at Site 1254 (see **"Lithostratigraphy,"** p. 13, in the "Site 1254" chapter), we interpret these blocks to be redeposited fragments of shallow-water carbonate emplaced on the lower trench slope within a muddy debris flow.

Carbonate Sediment

The proportion of carbonate material in the sediment recovered at Site 1255 is low (<5% according to smear slide analysis and shipboard chemical analysis) (see **"Organic Geochemistry,"** p. 18), but in one location in interval 205-1255A-3R-2, 141–146 cm (145.31 mbsf), there is a unit of nannofossil chalk with clay, deformed by drilling and located immediately below the sandy unit at the top of lithostratigraphic Sublayer U1A (Fig. **F12**). The chalk itself is structureless but is underlain by a thin interval of planar laminated clay. In microscopic analysis the sediment is revealed to be largely composed of nannofossils and especially *Discoasters* (Fig. **F8C**) with minor volumes of clastic material (palagonitized volcanic glass, quartz, opaque minerals, and mica). The deposit is apparently a pelagic interval within the dominantly redeposited facies of lithostratigraphic Subunit U1A.

Because the bulk of the biogenic input into this sequence is siliceous and there is no evidence for redeposition of this bed, the presence of the chalk interval must reflect a brief deepening of the carbonate compensation depth (CCD). Van Andel (1975) placed the recent Pacific CCD close to 4.5 km depth, although it may be as much as 1 km shallower in regions of upwelling and close to continental margins, as is the case here (Balsam, 1982). The presence of a pelagic carbonate bed of this type thus represents a major, albeit brief, excursion in the chemistry and productivity of the Costa Rican margin.

F10. A redeposited conglomeratic layer, p. 31.

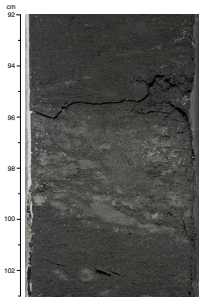

F11. Cobble of lithified limestone, p. 32.

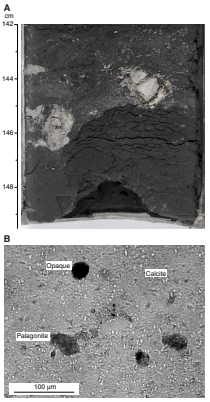

F12. Lithologic variation below the Unit T1/Subunit U1A lithostratigraphic boundary, p. 33.

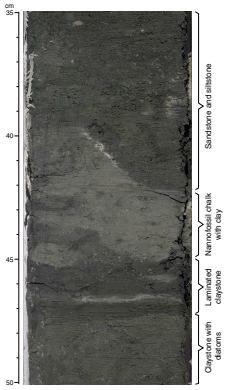

Volcanic Material

Unlike other sites drilled during Leg 205, the sediments at Site 1255 contain no primary volcanic tephra beds. However, volcanic material does comprise a significant proportion of the clastic sediments, which are largely derived from the erosion of the Costa Rica volcanic arc. Smear slide analysis shows 10%–15% to be the typical range for the proportion of either fresh volcanic glass shards, palagonitized glass, or zeolites formed from the alteration of volcanic glass. Locally, that proportion can increase to >25%, with specific intervals being found in Sections 205-1255A-2R-1, 10 cm (132.80 mbsf); 2R-3, 6 cm (134.48 mbsf); and 3R-1, 0 cm (142.40 mbsf). A compilation of the smear slide information from Sites 1043 and 1255 shows that although volcanic glass is present in both wedge and underthrust sediments, it is most abundant in the forearc wedge sediments (Fig. F8).

Diagenesis

Diagenesis at Site 1255 seems to be developed to a similar degree in both forearc wedge and underthrust sediments. The sediment is firm and weakly indurated but not yet fully lithified, equivalent to a chalk grade for carbonate sediments. An exception to this lies in interval 205-1255A-2R-1, 0–15 cm (132.70 mbsf), where a cobble of well-lithified massive dark brownish gray siltstone is recognized (Fig. F13). This block is carbonate cemented and may not be in place, coming at the top of the recovered interval.

Sediment Geochemistry

Major and trace element analyses of three sediment samples were conducted aboard ship following the methods described in "Igneous Petrology," p. 11, in the "Explanatory Notes" chapter. Major, minor, and trace element analyses are presented in Table T2. Analyses were made on freeze-dried bulk samples that are a mixture of sediment particles and sea salts (see "Igneous Petrology," p. 11, in the "Explanatory Notes" chapter). The data have not yet been corrected for porosity and pore water contribution to the bulk sediment composition. Major element concentrations show no discernable downsection trend and lie within the range of values determined from across the décollement at Sites 1040 and 1254. There is no sediment chemistry available from the closest borehole at Site 1043.

In terms of the trace element composition, a pattern is discernable across the lithostratigraphic unit boundary at 144.08 mbsf. Barium, and to a lesser extent Ni, increase downsection into lithostratigraphic Subunit U1A. This pattern was observed at Sites 1040 and 1254, where Ba concentrations average 426 ppm above the décollement but shift to an average value of 1575 ppm for samples below that level. This is consistent with the proposed location of the unit boundary between intervals 205-1255A-2R-2, 0–3 cm, and 3R-2, 87–127 cm. High concentrations of Ba can be driven by the presence of volcanic materials in the sediment. However, the lack of any change in the SiO_2 and K_2O concentrations, together with the smear slide analyses, suggest that volcanic material content is not a key control on the Ba chemistry in this case. We interpret the increased Ba concentration in the sediment below the unit boundary to reflect higher authigenic Ba within lithostratigraphic Subunit U1A.

F13. Cobbles of lithified siltstone, p. 34.

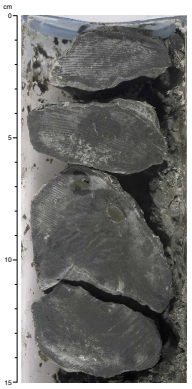

T2. Bulk geochemical analysis, Site 1255, p. 45.

X-Ray Diffraction

The results of X-ray diffraction (XRD) analyses of randomly oriented bulk sediment powders from Leg 170 Site 1043 and Leg 205 Site 1255 are presented. Shipboard Leg 170 XRD data were not evaluated previously, nor were mineral peaks identified. Data from Leg 170 diffractograms were analyzed for the first time during Leg 205 and are thus considered here. Site 1043 peak intensity and peak area data are listed in Table T3, and peak area ratios are listed in Table T4. Site 1255 peak intensity and peak area data are listed in Table T5, and relative abundance data are listed in Table T6.

T3. XRD analysis, Site 1043, p. 46.

T4. Peak area ratios of dominant minerals, Hole 1043A, p. 47.

T5. XRD analysis, Site 1255, p. 48.

T6. Peak area ratios of dominant minerals, Hole 1255A, p. 49.

Summary

The section recovered from Hole 1255A can be readily split into lithostratigraphic Unit T1 and Subunit U1A at the level of 144.08 mbsf. The division marks the sharp junction between a series of claystones with silts and low or no diatoms above and an underlying series of diatom-rich claystones with interbedded silts, sands, and even occasional fine-grained conglomerates. The clastic sediments in the underthrust section (Subunit U1A) differ from the purely hemipelagic diatom ooze recorded at Site 1043 (Subunit U1B), although the degree of recovery and uncertainties in the precise depth within the cored interval from which these sediments were taken are sufficient to suggest that these sediments may have been developed at Site 1039 but simply not recovered. Blocks of reworked carbonate in the overlying lithostratigraphic Unit T1 indicate that these sediments are mostly debris flows, derived originally from shallow nearshore environments. The underthrust section represents a trench depositional setting with turbidite silts and sands interbedded with biogenic hemipelagic mudstones.

STRUCTURAL GEOLOGY

Coring at Site 1255 began at 123 mbsf with the target to recover the décollement as recognized at Site 1043 (Kimura, Silver, Blum, et al., 1997). From the first core recovery at 132.7 to 144.08 mbsf, sediments exhibit a downward increase in deformation intensity. Deformation is characterized by brecciation and polished clast surfaces, indicating an incipient scaly fabric (Fig. F14). The top of the décollement could not be defined because of the limited cored interval and poor recovery, but its base is sharp and well defined (Fig. F15). This lower boundary also coincides with the contact between Unit T1 and Subunit U1A as described at Site 1043 (Kimura, Silver, Blum, et al., 1997). At Site 1043, spiraliferous drilling disturbance was observed; this was not observed at Site 1255, although other types of drilling disturbance affected some intervals (Fig. F14). Only one measurement of bedding dip was possible in the décollement zone (44°).

The underthrust section starts at Section 205-1255A-3R-2, 18 cm (144.08 mbsf), and is characterized by alternating turbiditic and hemipelagic clay-rich layers. The clay-rich layers exhibit some brecciation with unpolished surfaces (Fig. F14), likely related to the shear zone, whereas the sandy layers are remarkably undeformed.

F14. Structural and lithologic summary, p. 35.

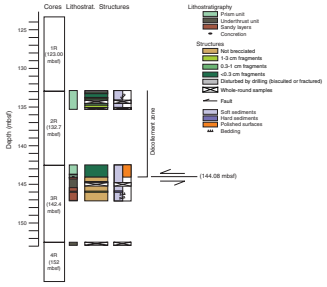

F15. Base of the décollement zone and Unit T1/Subunit U1A lithologic boundary, p. 36.

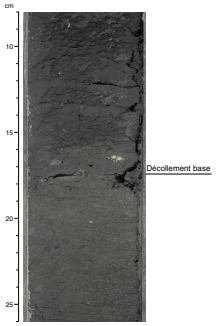

PHYSICAL PROPERTIES

At Site 1255, laboratory measurements were made to provide a profile of physical properties across the décollement, which was previously cored in Hole 1043A and logged by LWD in Hole 1043B. All cores were initially passed through the multisensor track (MST) before being split. Gamma ray attenuation (GRA) bulk density and volumetric magnetic susceptibility measurements were taken at 4-cm intervals, with measurements averaged from three separate 1-s data acquisitions for all cores. *P*-wave velocity logger measurements were not taken because of the small and variable diameter of RCB cores that generally leads to poor coupling between the core liner and recovered core. Natural gamma radiation (NGR) was counted every 10 cm for 20-s intervals. No *P*-wave velocity or thermal conductivity measurements were made at this site because the cores were unsuitable.

Moisture and density samples were selected from undisturbed core at regularly spaced intervals of two per full section (75-cm resolution). Measurements of dry volume and wet and dry mass were uploaded to the ODP Janus database and were used to calculate water content, bulk density, grain density, porosity, void ratio, and dry bulk density. Calculated physical property data are available from the ODP Janus database for all MST and moisture and density measurements.

Density and Porosity

Porosity values determined from moisture and density measurements vary from 51.8% to 65.3% and are consistent with data from Site 1043 (Fig. F16A). Bulk densities range from 1.61 to 1.81 g/cm³ (Fig. F16B). GRA densities show significant scatter (Fig. F16C). Grain densities (Fig. F17) vary from 2.59 to 2.75 g/cm³ and are consistent with those from Site 1043.

Natural Gamma Radiation

NGR results are presented in counts per second (cps) (Fig. F18). The background, produced by Compton scattering, photoelectric absorption, and pair production (12.95 cps), was measured at the beginning and during MST runs for each core section. Because Site 1043 background corrections are not available, Figure F18 shows uncorrected values for both Sites 1255 and 1043. In Core 205-1255A-2R, NGR counts range from 21 to 34 cps (corrected values of 8–21 cps), and in Core 3R, NGR counts range from 26 to 44 cps (corrected values of 13–31 cps). NGR values appear to increase with depth and are consistent with those from Site 1043.

Magnetic Susceptibility

Volumetric magnetic susceptibility measured with the MST shows generally low values in Core 205-1255A-2R and in the top 2 m of Core 3R (Fig. F19). Below 144.5 mbsf, values increase significantly. This increase corresponds to a transition from silty mud to sandier material with some conglomerates, as noted in core description (see "Lithostratigraphy," p. 7). Values between 143 and 144 mbsf differ between Sites 1255 and 1043. This could reflect either depth discrepancies result-

F16. Porosity, bulk density, and corrected GRA and moisture and density bulk densities, p. 37.

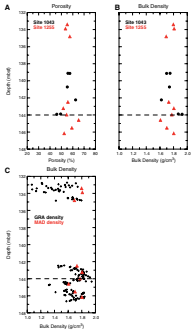

F17. Grain densities, p. 38.

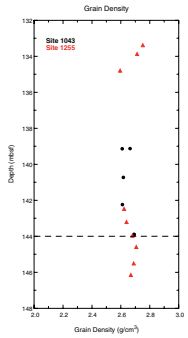

F18. Uncorrected MST NGR measurements, p. 39.

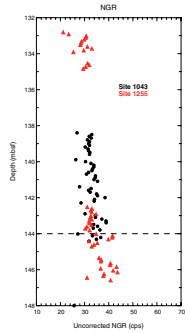

F19. MST volumetric magnetic susceptibility, p. 40.

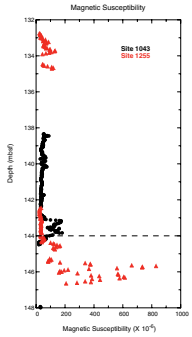

ing from incomplete core recovery or lithologic variations between the sites.

PALEOMAGNETISM

Demagnetization of natural remanent magnetization (NRM) in archive-half cores and discrete samples was performed to identify polarity changes and to provide data for reorientation of intact core pieces, despite poor recovery of RCB cores. The archive sections of the core were progressively demagnetized at 2-cm intervals using alternating-field (AF) demagnetization up to 40 mT in increments of 10 mT, and occasionally strong AF demagnetization of 45 to 60 mT in increments of 5 mT was applied for investigating polarity changes. Discrete samples were selected from undisturbed core pieces and demagnetized up to 80 mT in increments of 5 mT.

Magnetic susceptibility was measured using a point sensor on the archive multisensor track (AMST) at 2-cm intervals and was compared to susceptibility of whole-round cores measured by the MST (see **"Physical Properties,"** p. 12) and to magnetic intensity data.

Paleomagnetism

Paleomagnetic declination and inclination of archive cores after 40-mT demagnetization and discrete results are shown in Figure **F20.** Rapid changes in the inclination and declination were observed in Core 205-1255A-2R from 132.76 to 134.84 mbsf (Sections 205-1255A-2R-1 through 2R-3). Relatively well defined sequences of negative inclinations with declination changes from 132.98 to 133.12 mbsf (interval 205-1255A-2R-1, 28–42 cm) are believed to indicate reversed magnetic polarity. From 133.46 to 134.80 mbsf (Sections 205-1255A-2R-1, 76 cm, through 2R-3, 38 cm), the inclinations show very shallow and wide declinations (Fig. **F20**). Disagreement of magnetic inclinations between the archive sections and the discrete samples in this interval indicate that these inclinations are questionable. Within Core 205-1255A-3R, a clear polarity change was identified from 144.15 to 145.38 mbsf (Sections 205-1255A-3R-2, 25 cm, through 3R-3, 15 cm) by significant direction changes of the magnetic declination and inclination observed in both archive sections and discrete samples (Fig. **F20**).

F20. Magnetic polarity changes of archive-half cores after 40-mT demagnetization, p. 41.

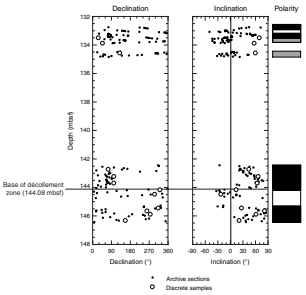

Magnetic Intensity

Relatively high magnetic intensities were observed within Core 205-1255A-2R, in which magnetic susceptibilities measured by the AMST and the MST are also slightly elevated (Fig. **F21**). High intensities also occur at ~143 mbsf; however, no corresponding changes in magnetic susceptibility are observed in this interval. A very small change in the magnetic intensity begins at 144.15 mbsf (Section 205-1255A-3R-2, 25 cm) with a slightly higher peak in the susceptibility, corresponding to the polarity boundary discussed above (Fig. **F20**). Significantly higher magnetic intensities below 145.58 mbsf (Section 205-1255A-3R-3, 55 cm) correspond to clear peaks in magnetic susceptibility (Fig. **F21**).

F21. NRM intensity and magnetic susceptibility of archive-half cores, p. 42.

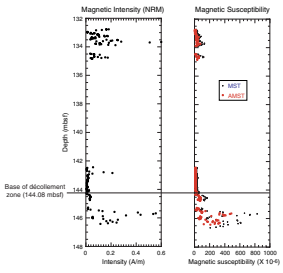

Conclusion

A short interval of negative polarity was identified from 132.98 to 133.12 mbsf (interval 205-1255A-2R-1, 28–42 cm). Polarity identification is not possible from 133.46 to 134.80 mbsf because of variable magnetic declinations and disagreements between archive cores and discrete data. A clear negative polarity associated with an intensity change is identified from 144.15 to 145.38 mbsf (Sections 205-1255A-3R-2, 25 cm, through 3R-3, 15 cm). This clear short negative polarity was not identified during the previous Leg 170 paleomagnetic study at Site 1043 (Kimura, Silver, Blum, et. al., 1997).

INORGANIC GEOCHEMISTRY

The main objectives for determining key geochemical parameters of the pore waters at Site 1255, ~1 km west of Site 1254 and closer to the deformation front, are the same as those for Site 1254 (see "Inorganic Geochemistry," p. 27, in the "Site 1254" chapter), with particular emphasis on the determination of the key depth interval in which to place the long-term geochemical observatory. Limited core recovery, however, permitted only a few samples to be measured, and interpretations should be regarded as preliminary. A total of three 38- to 43-cm-long whole rounds were sampled at Site 1255 for pore fluid geochemistry. One whole round was taken per core from 134.2 to 152.2 mbsf, and pore water recovery ranged from 14 to 46 mL. Pore waters were analyzed for Ca, Mg, K, Na, B, Ba, Fe, Mn, Sr, Si, NH_4, SO_4, and alkalinity concentrations, as well as for pH and salinity by methods described in "Inorganic Geochemistry," p. 24, in the "Explanatory Notes" chapter. Pore water geochemistry data is shown in Tables T7 and T8.

T7. Pore water major constituents, Site 1255, p. 50.

T8. Pore water minor constituents, Site 1255, p. 51.

Lithium, Ca, K, Mg, and Na were analyzed in "real time" on the shipboard inductively coupled plasma–atomic emission spectrophotometer to facilitate identification of the zone of maximum fluid flow within the décollement, as was done at Site 1254. Potassium, Na, and Ca concentrations at Site 1043 (Leg 170) decrease abruptly at the top of the décollement, whereas Mg concentrations increase. These constituents show opposite gradients within the transition from the décollement to the underthrust sediments. Therefore, the objective of real-time chemical monitoring for these constituents was to quickly identify these concentration gradients to ensure that the underthrust sediments were not penetrated too deeply during coring, such that the long-term observatory will sample décollement fluid and not a mixture of décollement and underthrust fluids. Because of the limited amount of core recovered at Site 1255, the real-time chemical analyses were not as successful as those at Site 1254; however, alkalinity and SO_4 could be determined fairly rapidly and were helpful in approximately determining the transition between the wedge sediments and underthrust sediments.

Pore Water Results

Salinity and Chloride

Salinity is below seawater concentration in all samples analyzed at Site 1255 (Table T7) and increases with depth from 32 (8.5% lower than seawater) at 134.2 mbsf to 34 (3% lower than seawater) at 152.2 mbsf in the underthrust sediments. The lithologic boundary between wedge

sediments and underthrust sediments occurs at 144.08 mbsf (see "Lithostratigraphy," p. 7), and the lower boundary of the décollement occurs at the same depth (see "Structural Geology," p. 11). As at Sites 1254 and 1043, the low salinity signature of the fluid within the décollement zone is interpreted as the result of advection of a low-salinity deeply sourced fluid from greater depth.

Chloride concentrations increase with depth from 549 mM (~2% lower than seawater concentration) within the décollement at 134.2 mbsf to seawater concentration within the transition between the deformed wedge sediments and the sediments of the underthrust section (Table T7). The low-chloride signature within the décollement at Site 1255 is less pronounced than the low-salinity signature and is most likely the result of mixing with a low-chloride deeply sourced fluid as observed at Sites 1254 and 1043.

Sodium and Potassium

Within the décollement, the Na concentration was calculated assuming alkalinity is very low (Kimura, Silver, Blum, et al., 1997). The calculated value is ~6% lower than seawater concentration. Sodium concentration increases to approximately seawater value within the underthrust sediment section at 145.8 mbsf (Table T7). Potassium concentrations are above seawater concentration in all three samples and range between 11.18 and 13.42 mM. There was not a sharp decrease in K concentrations within the décollement as observed at Site 1043, which suggests that the samples from Site 1255 were not within the zone of the minimum concentration of 8.8 mM, observed at 142.45 mbsf at Site 1043.

Calcium, Magnesium, and Strontium

Calcium concentrations are below seawater concentration and increase with depth from 4.66 mM (56% lower than seawater) at 134.2 mbsf to 8.45 mM (20% lower than seawater) at 152.2 mbsf. At Site 1254, Ca concentrations within the décollement were approximately twice seawater concentration suggesting migration of a deeply sourced fluid through conduits within the décollement and upper fault zone (see "Inorganic Geochemistry," p. 27, in the "Site 1254" chapter). At Site 1255, pore waters from the limited amount of core recovered do not show evidence for the high-Ca deeply sourced fluid sampled at Site 1254 in the lower part of the wedge section. This difference between sites may simply reflect low resolution as a result of poor recovery, although mixing between pore fluids of the uppermost few meters of the underthrust hemipelagic sediment section and pore fluid from the lower wedge sediments is a possible explanation.

In the one sample recovered from the wedge sediments (134.2 mbsf), the Mg concentration is 38.08 mM (29% lower than seawater concentration). An increase in Mg concentrations to 46.05 mM at 145.8 mbsf reflects the transition between wedge sediments and the underthrust hemipelagic sediments. Also, the lower Mg concentration within the décollement provides evidence for infiltration of the deeply sourced fluid, sampled at Site 1254, into the décollement at Site 1255. Furthermore, the higher Mg concentrations in the décollement at Site 1255 compared to those at Site 1254 (16–18 mM) suggest mixing between pore fluids of the underthrust sediments with those of the lowermost

wedge sediments, or they may be the result of low resolution resulting from poor core recovery.

Strontium concentrations are variable within the depths sampled at Site 1255 and range between 94.76 and 98.42 µM. (Table T8).

Sulfate, Alkalinity, Ammonium, and Barium

Sulfate concentrations are zero within the lower wedge sediments at Sites 1255 and 1043. Sulfate concentrations increase sharply between 134.2 and 145.8 mbsf from 0 to 8.01 mM, reflecting the transition to the underthrust sediment section. Correspondingly, methane concentrations are high throughout the wedge section and are at background levels below the décollement (see "Organic Geochemistry," p. 18). At Site 1255, the uppermost underthrust sediments have been isolated from the external supply of dissolved SO_4 from seawater and the remaining internal supply of SO_4 at the top of the section has been mostly but not completely depleted by bacteria to concentrations of 7.25 mM at 145.8 mbsf and 8.61 mM at 152.2 mbsf (25% to 30% of seawater concentration, respectively), reflecting the location of Site 1255 (closer to the deformation front than Site 1254) where SO_4 in the underthrust sediments was completely exhausted. Alkalinity concentrations at Site 1255 are high and range from 18.422 mM (8 times seawater alkalinity) to 22.645 mM (~10 times seawater alkalinity), which contrasts with Site 1040, where the alkalinity values are low (~5 mM) in the lower wedge section and immediately above the décollement. These high concentrations most likely result from mixing with the high alkalinity pore fluids that are characteristic of the uppermost hemipelagic section at Site 1039.

Ammonium concentrations decrease with depth from 2943.1 µM at 134.2 mbsf to 643.1 µM at 152.2 mbsf, which may reflect decreasing sedimentary organic matter content with depth. Barium concentrations in pore fluids from the wedge sediments at Site 1255 are similar to those at Site 1254 (~9.3 µM Ba); however, Ba in the underthrust sediment pore fluids increases sharply to 160 µM at Site 1254, whereas Ba concentrations decrease abruptly to 3.2 µM at 152.2 mbsf at Site 1255. At Site 1254, SO_4 depletion (i.e., SO_4 = 0 mM) extends into the underthrust sediments, but at Site 1255, SO_4 concentrations in the underthrust increase to 8.61 mM at 152.2 mbsf. Therefore, the decrease in Ba concentration within the underthrust sediment pore fluids at Site 1255 may be due to barite precipitation.

Iron and Manganese

Iron concentrations are variable at Site 1255 and range between 3.34 and 8.34 µM. The highest Fe concentrations are present right below the boundary between the wedge sediments and underthrust sediments at a depth of 145.8 mbsf (see "Lithostratigraphy," p. 7) and may represent bacterial reduction of $Fe(OH)_3$ within the uppermost underthrust sediments. Manganese concentrations increase with depth and range between 2.97 µM at 134.2 mbsf and 26.08 µM at 152.2 mbsf. The increase in Mn concentrations reflects the transition between wedge sediments and underthrust sediments. Sulfate has not been totally depleted in the upper underthrust section as at Site 1254, and active reduction of MnO_2 may be occurring, which may keep dissolved Mn concentrations relatively high.

Lithium, Silica, and Boron

Lithium concentrations decrease with depth from 32.89 µM (22% higher than seawater) at 134.2 mbsf to 26.69 µM (approximately seawater concentration) at 152.2 mbsf. The higher than seawater Li concentration observed within the wedge sediments is similar to that observed at the base of the décollement at Site 1254 and suggests infiltration of a deeply sourced fluid within the décollement at Site 1255. The decrease to approximately seawater concentration between 134.2 and 152.2 mbsf reflects the transition from wedge sediments to the hemipelagic sediments of the underthrust section.

Silica concentrations are relatively high at Site 1255 and increase with depth from 623.9 µM at 134.2 mbsf to 717.9 µM at 152.2 mbsf. The increase in Si concentrations with depth is due to the dissolution of diatoms and radiolarians that are abundant in the underthrust sediments but more rare in the décollement sediments. However, Si concentrations in the décollement at Site 1254 range from 51.4 to 61.4 µM, which is only 9% the concentration observed at Site 1255; Si concentrations within the underthrust sediments at Site 1254 range from 553 to 549 µM, which is 88% of the concentration observed in underthrust sediments at Site 1255. The discrepancy in Si concentrations between the two sites may reflect differing amounts of diatoms within the sediments (see **"Lithostratigraphy,"** p. 7; also see **"Lithostratigraphy,"** p. 13, in the "Site 1254" chapter) or may be due to mixing between pore fluids from the uppermost few meters of the hemipelagic sediments with pore fluid from the lower wedge sediments at Site 1255 but not at Site 1254.

Boron concentrations range from 352.9 µM (22% lower than seawater concentration) at 134.2 mbsf to 624.67 µM (39% higher than seawater concentration) at 152.2 mbsf, which reflects the transition from deformed wedge sediments to sediments of the underthrust section.

Discussion

As we observed at Site 1254, the chemical compositions of the pore fluids at Site 1255 are distinctly different in the wedge and underthrust section, with a less-sharp transition at the base of the décollement zone at ~144 mbsf. Fluid flow is suggested by salinity, Cl, Na, and Mg concentration minima and a Li concentration maximum within the décollement sample at 134.2 mbsf. These concentration minima were observed at Site 1043 along with a Mg concentration maximum within the same interval. Across the décollement, the shift in concentrations of some chemical components is reversed from the gradients observed at Site 1254 (i.e., Ca and Mg). In general, the pore fluids within the upper fault zone and in the décollement at Sites 1254 and 1040 are characterized by having a significantly stronger signature of a deeply sourced fluid than the pore fluids from Sites 1255 and 1043 (see **"Inorganic Geochemistry,"** p. 27, in the "Site 1254" chapter). At Sites 1255 and 1043, the pore fluid chemistry in the wedge and the uppermost underthrust sediments can be attributed to sampling mixing between the lower wedge and uppermost hemipelagic pore fluids, therefore, partially obscuring the deeply sourced fluid signature observed at Site 1254.

ORGANIC GEOCHEMISTRY

The main objectives for Site 1255 with respect to the organic geochemistry were similar to those at Site 1254. They are (1) characterizing the hydrologic system along the décollement observed during Leg 170 at Site 1043; (2) determining the chemistry and composition of pore fluids and gases from the décollement to compare with profiles measured during Leg 170 and to evaluate possible spatial heterogeneity and any possible changes through time for diagenetic and hydrologic modeling; (3) constraining pathways of fluid return to the surface and to evaluate the effects of this flow system on element fluxes; and (4) determining the target horizon for long-term fluid flow monitoring. Because of time constraints, only limited coring was attempted (four cores from 123 to 157 mbsf, with recovery between 132.7 and 152.6 mbsf) for determining the horizon to target long-term fluid flow monitoring. However, limited core recovery permitted only a few samples to be measured, and interpretations should be regarded as preliminary.

Gas Results

Volatile Hydrocarbons

At the prism Site 1255, volatile hydrocarbon gases (primarily methane, ethane, and propane) were sampled by headspace and vacutainer techniques and analyzed by gas chromatography (see **"Organic Geochemistry,"** p. 26, in the "Explanatory Notes" chapter). Headspace and vacutainer samples were taken and analyzed as soon as possible to allow for "real-time" monitoring. Headspace results are summarized in Table **T9** and shown in Figure **F22,** and vacutainer data are compiled in Table **T10.**

In contrast to the cores at Site 1254, no gas voids were apparent at Site 1255 and, hence, the gas samples taken with vacutainers show generally low methane concentrations but large contamination with air (Table **T10**), a result of the very low sediment recovery (7 m out of 34 m of core) as well as core disturbance from RCB drilling; both conditions facilitate loss of methane and aeration of the voids in the core. Therefore, at this site, the results of the headspace samples are preferred over the vacutainer data.

Headspace methane concentrations were high (>3000 ppmv) in Core 205-1255A-2R (132–135 mbsf) and then dropped drastically to ~5 ppmv at ~145 mbsf (Section 205-1255A-3R-2). Ethane concentrations are ~1000 times lower and disappear totally at ~144 mbsf. Based on the data from Sites 1254, 1040, and 1043 (Kimura, Silver, Blum, et al., 1997), propane was chosen as an indicator for flow from deeper sediment layers through the flow conduit system along the décollement (see also **"Organic Geochemistry,"** p. 33, in the "Site 1254" chapter). Propane was present but concentrations were low (~1 ppmv) at 132–135 mbsf and completely absent at greater depths. Higher hydrocarbons could not be detected in the gas samples. Compared to Site 1043, headspace hydrocarbon concentrations were constantly lower but showed a similar trend in the respective depth interval. Unfortunately, at both Sites 1254 and 1255, recovery was very low and, hence, the assigned depths at this site are approximate values and only comparable to Site 1254 data within a few meters (e.g., Core 205-1255A-2R could shift 7.12 m, Core 3R could shift 5.21 m, and Core 4R could shift 9 m). From the K, Ca, Mg, and Na data (see **"Inorganic Geochemistry,"**

T9. Headspace gas composition, p. 52.

F22. Headspace gas analyses, p. 43.

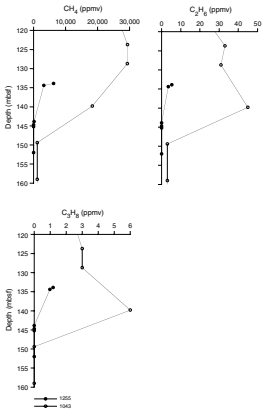

T10. Vacutainer gas composition, p. 53.

p. 14) it can be inferred that Core 205-1255A-2R lies above the décollement as determined at Site 1043 (Kimura, Silver, Blum, et al., 1997), whereas the decrease in hydrocarbon concentrations takes place across the lithologic boundary between prism and underthrust sediments at 144.08 mbsf (see "Structural Geology," p. 11).

The CH_4/C_2H_6 ratio for two samples only (Table T9) shows values of ~1000 above the lithologic boundary, indicating migrated thermogenic hydrocarbons (e.g., propane).

Sediment Results

Inorganic Carbon, Organic Carbon, and Total Sulfur

The results of inorganic carbon (reported as calcium carbonate), organic carbon, nitrogen, and sulfur measurements in the solid phase from the cores of Hole 1255A are reported in Table T11 (for details see "Organic Geochemistry," p. 26, in the "Explanatory Notes" chapter). In agreement with Site 1043 data, calcium carbonate concentrations are generally low (<5 wt%) in the cored intervals (i.e., in the prism as well as the uppermost underthrust). For the prism sediments, the total organic carbon (TOC) content shows values (~1 wt%) similar to those at Site 1043 (~1.4 wt%). In the uppermost underthrust sediments, the TOC content increases to the high surface concentrations (~1.7 wt% in Section 205-1255A-4R-1) observed at Site 1039 and also observed at Site 1043 below the décollement (Kimura, Silver, Blum, et al., 1997). Total sulfur (TS) concentrations are ~0.4 wt% in the prism sediments and, thus, lower than those at Site 1043 (however, the accuracy of the TS data was very poor); they increase to 1.0 wt% in the underthrust sediments.

T11. $CaCO_3$, total carbon, TOC, TN, and TS contents, p. 54.

Composition of Organic Matter

To characterize the type of organic matter in the sediments, total organic carbon/total nitrogen (TOC/TN) values and hydrogen index (HI) values from Rock-Eval pyrolysis have been used. Unfortunately, the S_3 channel of the Rock-Eval did not record any data and, hence, no oxygen index or S_2/S_3 ratio could be calculated (Table T12).

T12. Rock-Eval data, p. 55.

The TOC/TN ratio ranges from 6 to 8 (Table T11) in the prism as well as the underthrust sediments, indicating a predominantly marine origin of the organic material. The Redfield ratio of 6.6 gives the typical average for marine organic matter. As at Site 1254, the low HI values (100–140 mg HC/g TOC) (Table T12) suggest a significant input of terrigenous material (Emeis and Kvenvolden, 1986). This was not observed at this site. The discrepancy is most probably due to analytical problems with the Rock-Eval instrument. However, lithologic variations cannot be excluded. The low content (~0.2) of pyrolizable carbon as well as the combination of temperatures of maximum hydrocarbon generation (T_{max}) <440°C and low production indices (production indices < 0.2) reflect organic matter that is immature for oil production.

MICROBIOLOGY

Two 5-cm-long whole rounds were taken adjacent to interstitial water whole rounds, in those sections of the core judged most intact (Samples 205-1255A-2R-2, 43–48 cm, and 3R-2, 127–133 cm). Two samples

(5 cm^3 each) were frozen at –80°C immediately after collection for postcruise ATP quantification and DNA assessment. Small samples (0.5 cm^3) from the same locations were fixed in 2% formalin solution for postcruise cell counting. Twice during coring, 40-mL samples of drilling fluid were collected as the fluid escaped the core liner, and these samples were also frozen promptly at –80°C; evaluation of the drilling fluid will constrain estimates of core contamination in terms of real cell numbers.

The chemical tracer was not deployed during coring in Hole 1255A, but fluorescent microspheres were deployed in every core and counted using epifluorescence microscopy, as described in **"Microbiology,"** p. 28, in the "Explanatory Notes" chapter. No microspheres were found in interior or exterior core samples, and the arrival of microspheres to the sampling sites is uncertain because of low recovery. Postcruise microbiological work will take this uncertainty into consideration.

REFERENCES

Balsam, W.L., 1982. Carbonate dissolution and sedimentation on the Mid-Atlantic continental margin. *Science,* 217:929–931.

Emeis, K.-C., and Kvenvolden, K.A., 1986. Shipboard organic geochemistry on *JOIDES Resolution*. *ODP Tech. Note,* 7.

Kimura, G., Silver, E.A., Blum, P., et al., 1997. *Proc. ODP, Init. Repts.,* 170: College Station, TX (Ocean Drilling Program).

Ranero, C.R., and von Huene, R., 2000. Subduction erosion along the Middle America convergent margin. *Nature*, 404:748–752.

Shipboard Scientific Party, 1997. Site 1043. *In* Kimura, G., Silver, E., Blum, P., et al., *Proc. ODP, Init. Repts.,* 170: College Station, TX (Ocean Drilling Program), 215–247.

van Andel, T.H., 1975. Mesozoic/Cenozoic calcite compensation depth and the global distribution of calcareous sediments. *Earth Planet. Sci. Lett.,* 26:187–194.

Figure F1. Drill sites occupied during Leg 205 are shown as large yellow circles and those during Leg 170 as small white circles. The segment of multichannel seismic profile BGR 99-44 (red line) across Sites 1255 and 1043 is shown in Figure F3, p. 24. Leg 170 drill sites were based on seismic profile CR-20 (yellow line). Bathymetric map is an integration of the compilation by Ranero and von Huene (2000) and Simrad data from E. Flueh (pers. comm., 2000). The plate convergence direction is N30°E (arrow).

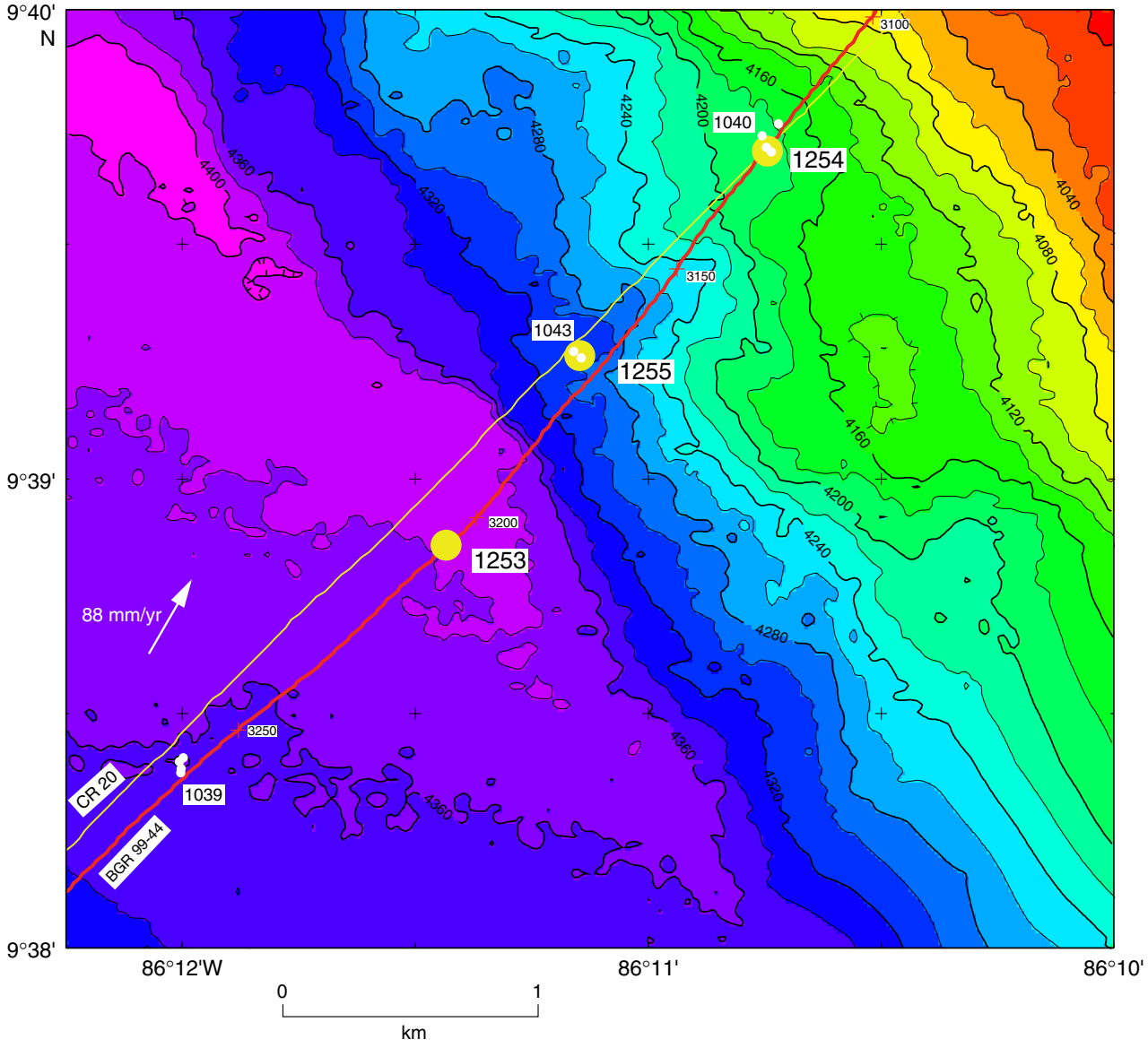

Figure F2. Location of Site 1255. Open circle = drill site occupied during Leg 205, solid circles = drill sites occupied during Leg 170. Bathymetric map is an integration of the compilation by Ranero and von Huene (2000) and Simrad data from E. Flueh (pers. comm., 2000).

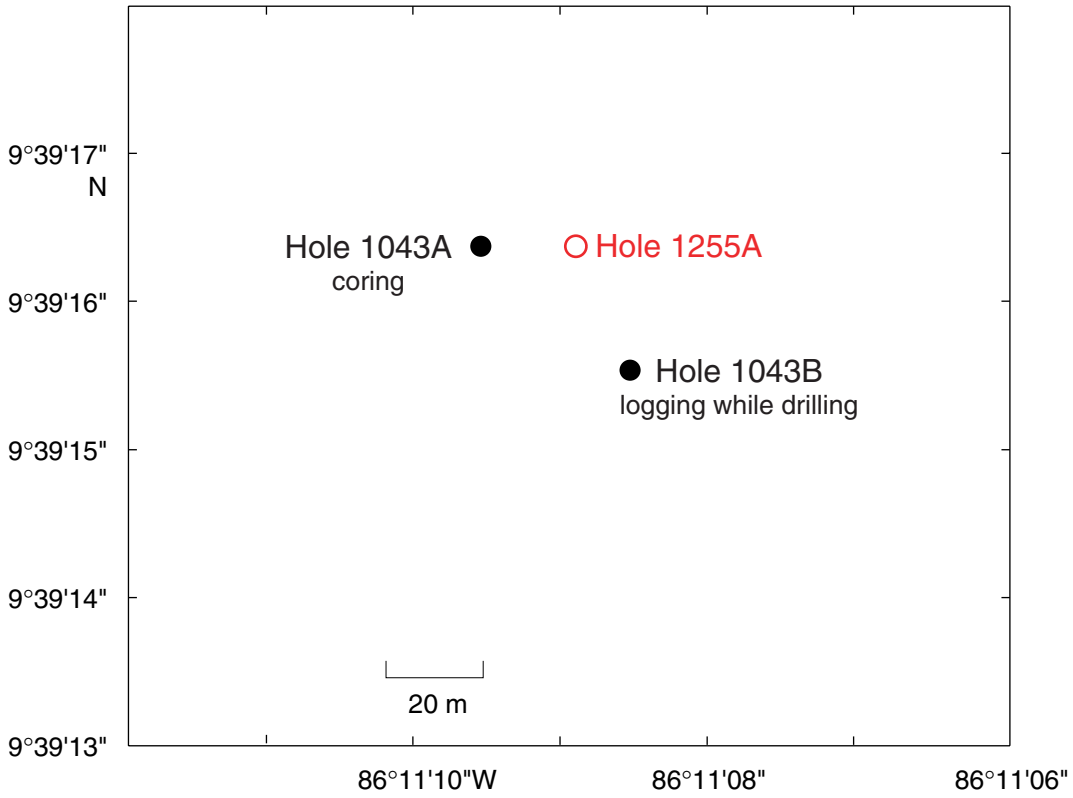

Figure F3. Portion of MCS profile BGR 99-44 across Sites 1255 and 1043. Location of seismic profile is shown in Figure F1, p. 22. Figure F23, p. 65, in the "Leg 205 Summary" chapter shows the BGR 99-44 seismic profile across all drill sites. Vertical exaggeration = 1.7. CMP = common midpoint.

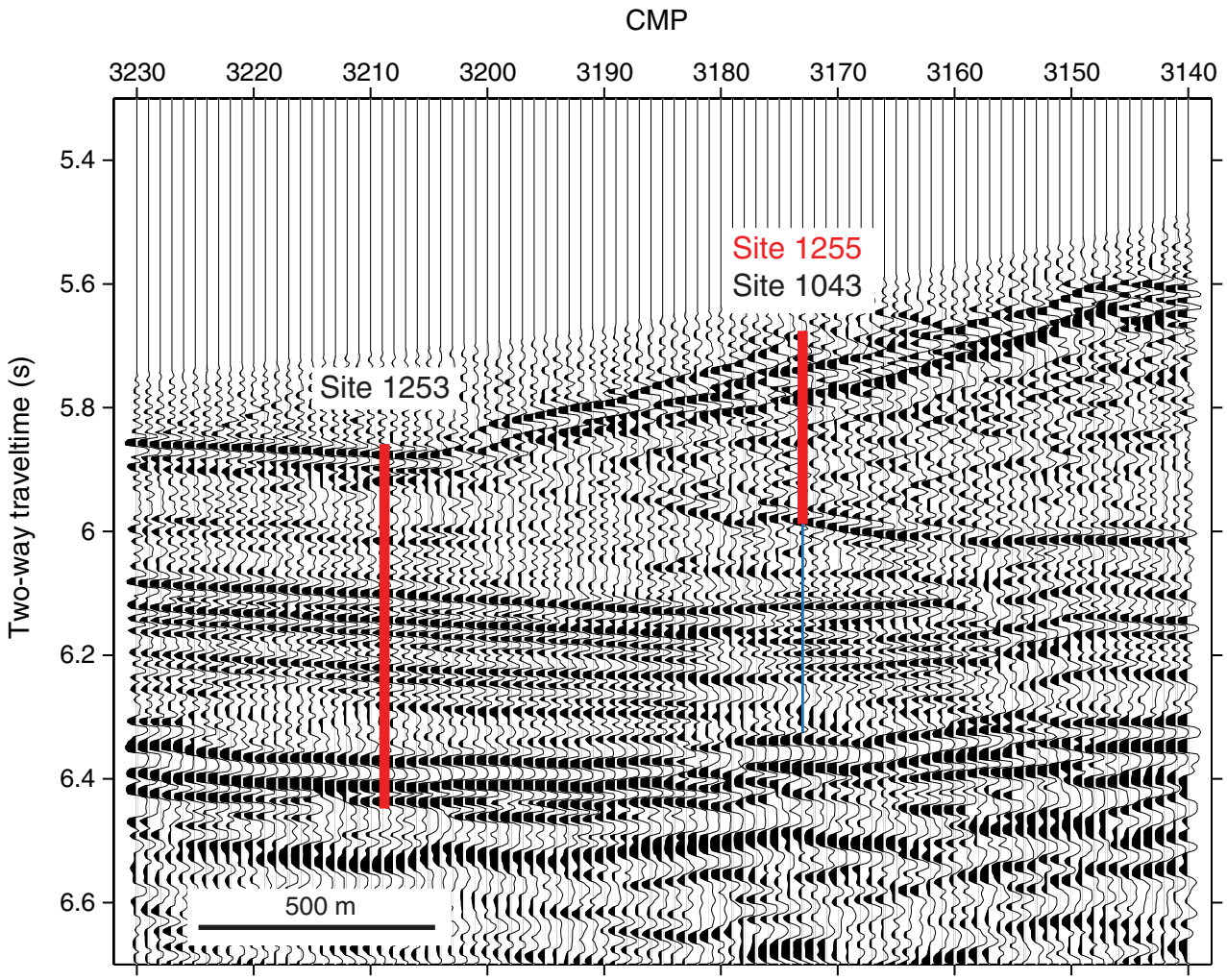

Figure F4. Hole 1255A CORK-II OsmoSampler installation space-out.

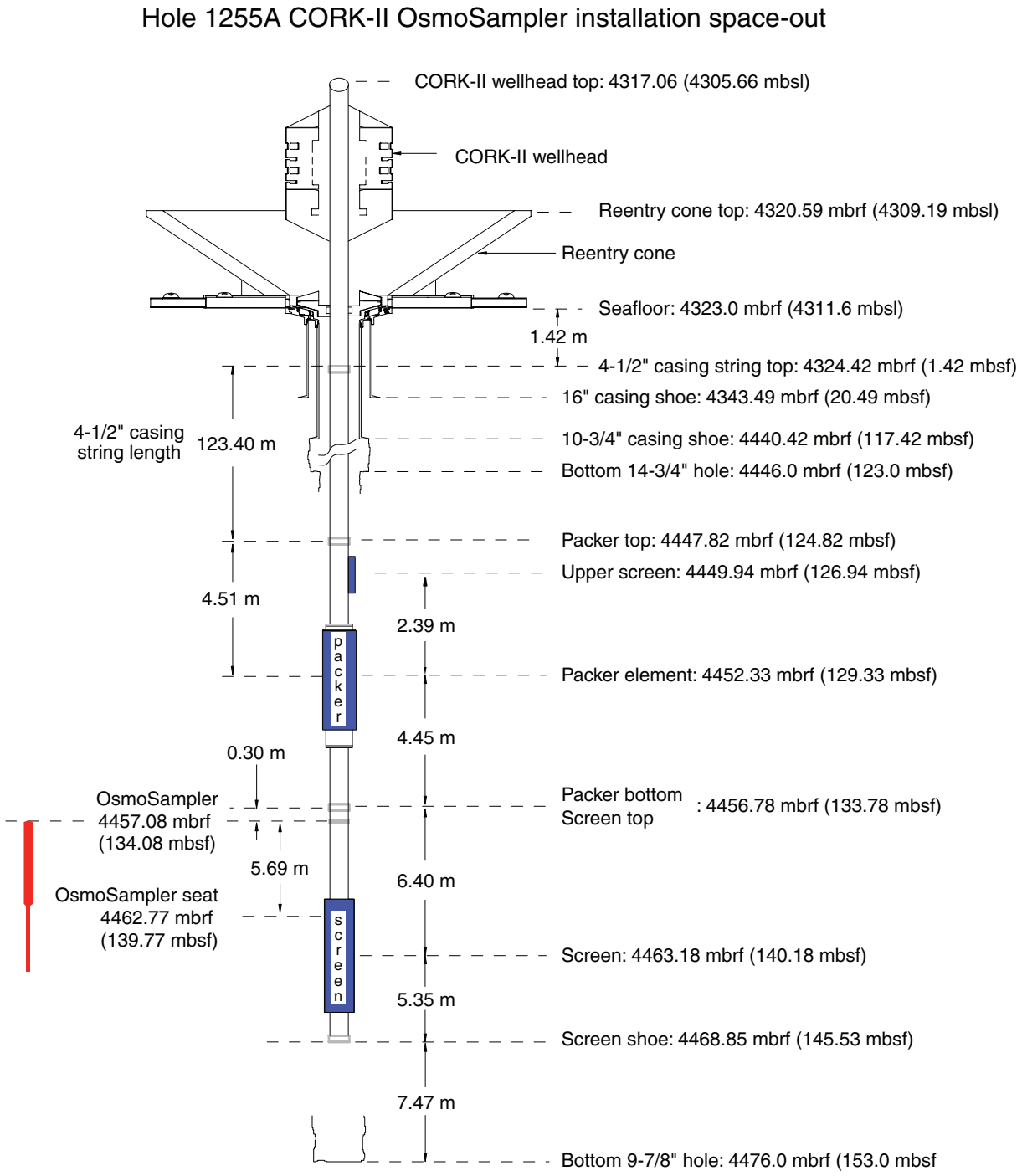

Figure F5. Composite stratigraphic log of the sedimentary section recovered at Sites 1043 and 1255 showing the degree of recovery, the principal stratigraphic units consistent with those defined by the Leg 170 scientific party, and the variation in lightness and chromaticity measured by the archive multisensor track. The color data plotted are only from Site 1043 because of the short length recovered at Site 1255 and the depth shift between the different sites.

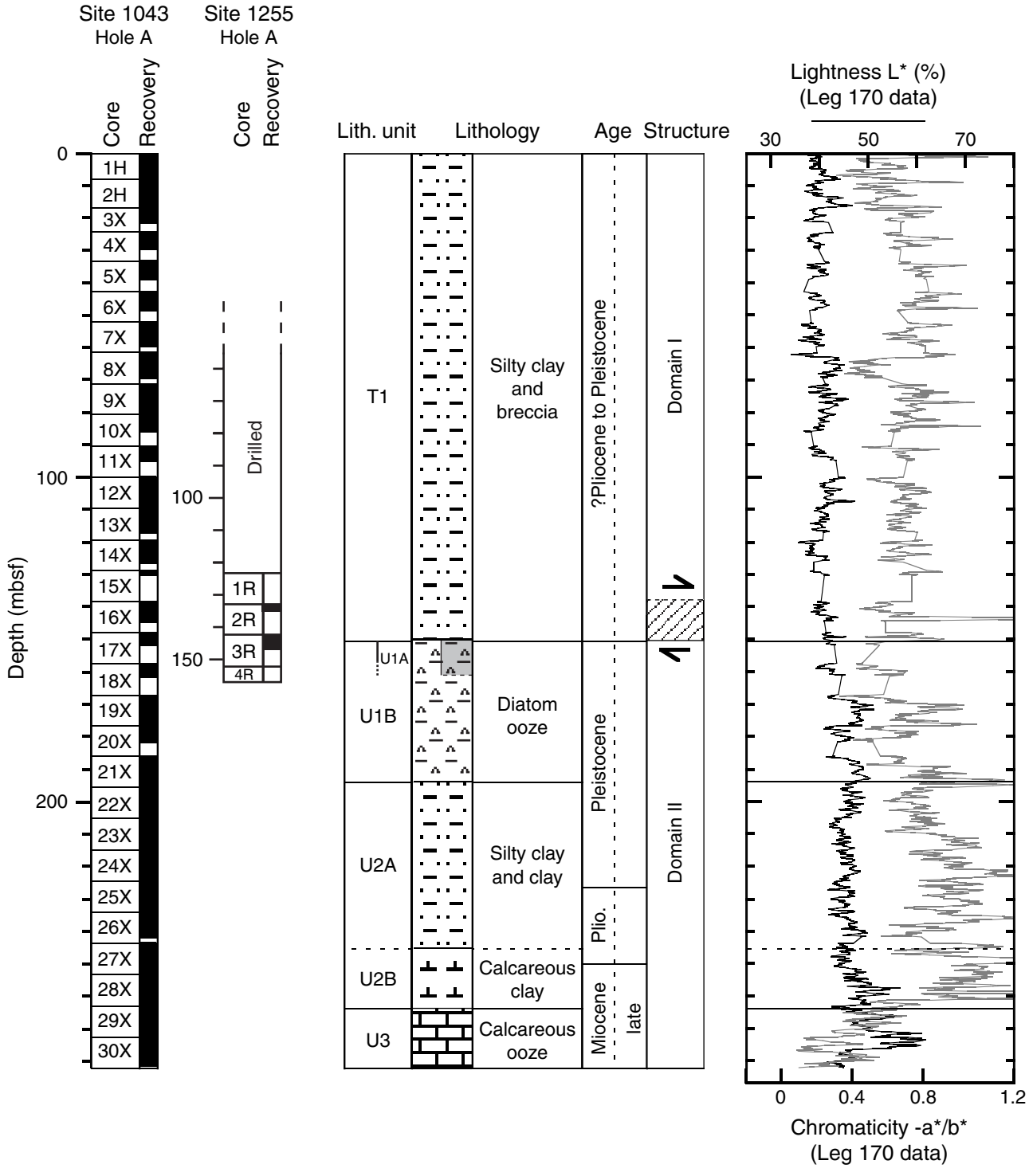

Figure F6. Close-up photograph of interval 205-1255A-3R-2, 53–70 cm. This interval, like much of the sediment at Site 1255, comprises fine-grained sediments with a variable proportion of clay that affects the color of the cut core surface.

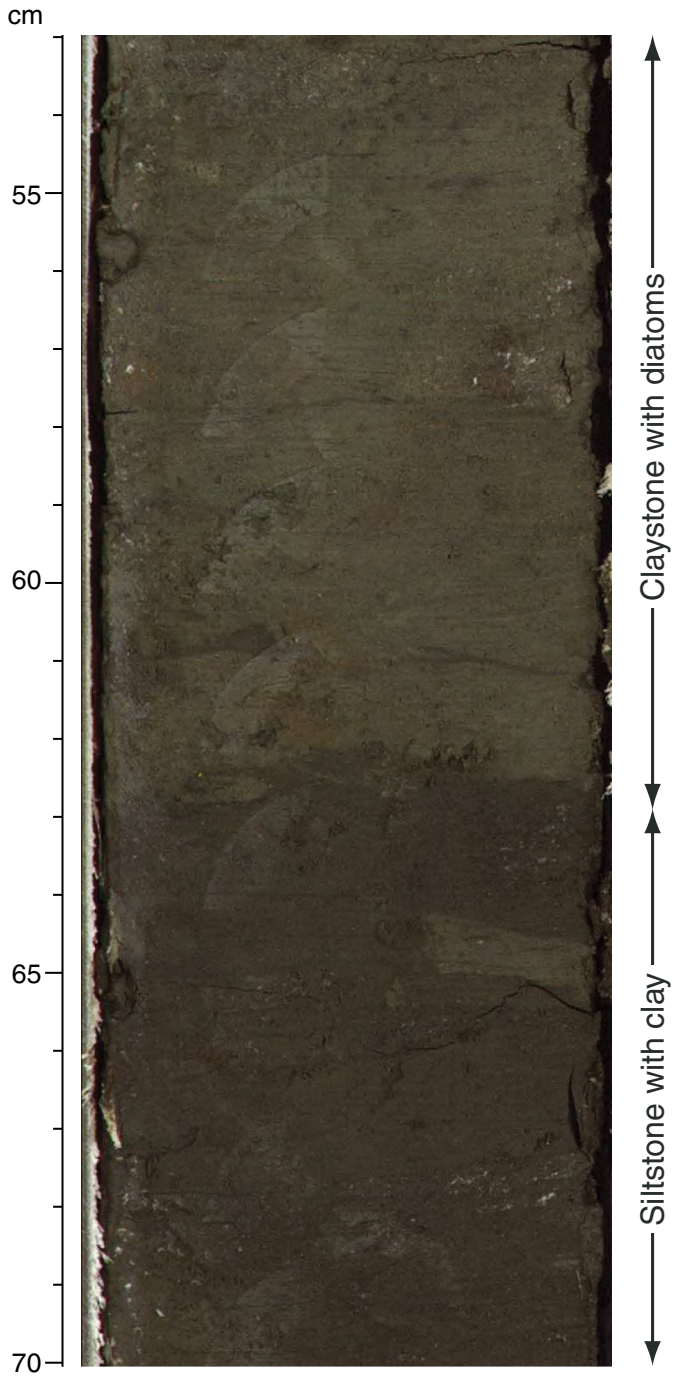

Figure F7. Compiled smear slide data for both Sites 1255 and 1043 from 0 to 300 mbsf. Points mark where the proportion of sand, clay, and volcanic glass are described as being abundant (>30%) and where the diatoms and nannofossils are defined as common or abundant (>15%).

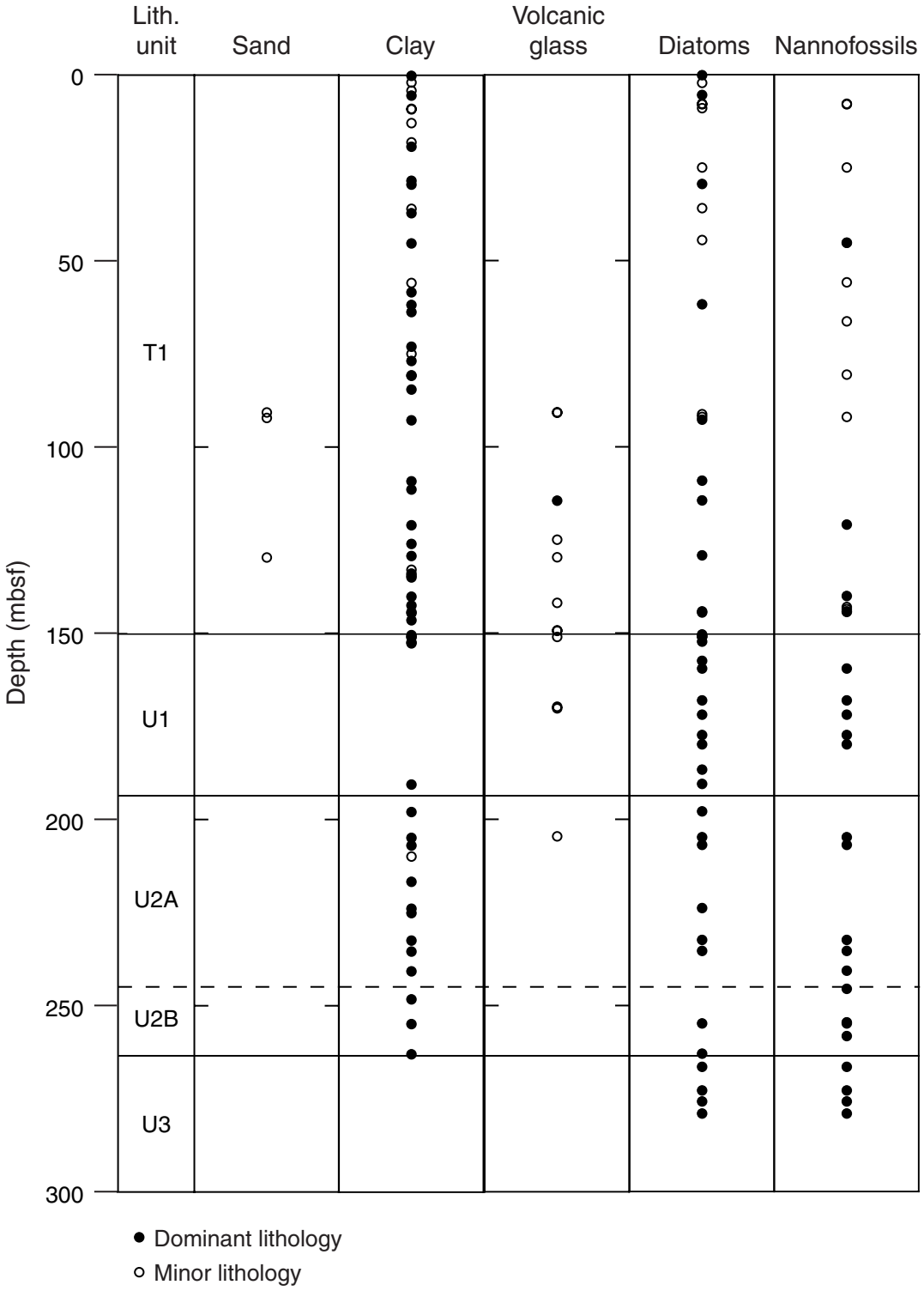

Figure F8. Photomicrographs of sediments recovered at Site 1255. **A.** Siltstone, a coarse-grained interbed within the otherwise clay-rich section (Sample 205-1255A-2R-1, 10 cm). **B.** Claystone with volcanic silt and minor amounts of diatoms just below the lithostratigraphic boundary (Sample 205-1255A-2R-CC, 1 cm). **C.** Nannofossil chalk with minor clays and silt (Sample 205-1255A-3R-2, 44 cm). Note the detrital mica grain and the many star-shaped *Discoaster*. **D.** Claystone with volcanic/palagonitic silt (Sample 205-1255A-3R-2, 71 cm). Note the abundant siliceous planktonic fauna of diatoms and silicoflagellates typical of underthrust lithostratigraphic Unit U1. **E.** Coarser redeposited material mixed with diatom-rich claystone (Sample 205-1255A-3R-CC, 1 cm). **F.** Large diatoms typical of lithostratigraphic Subunit U1B (Sample 205-1255A-4R-1, 1 cm). The clastic component is dominated by volcanic detritus or its altered equivalent.

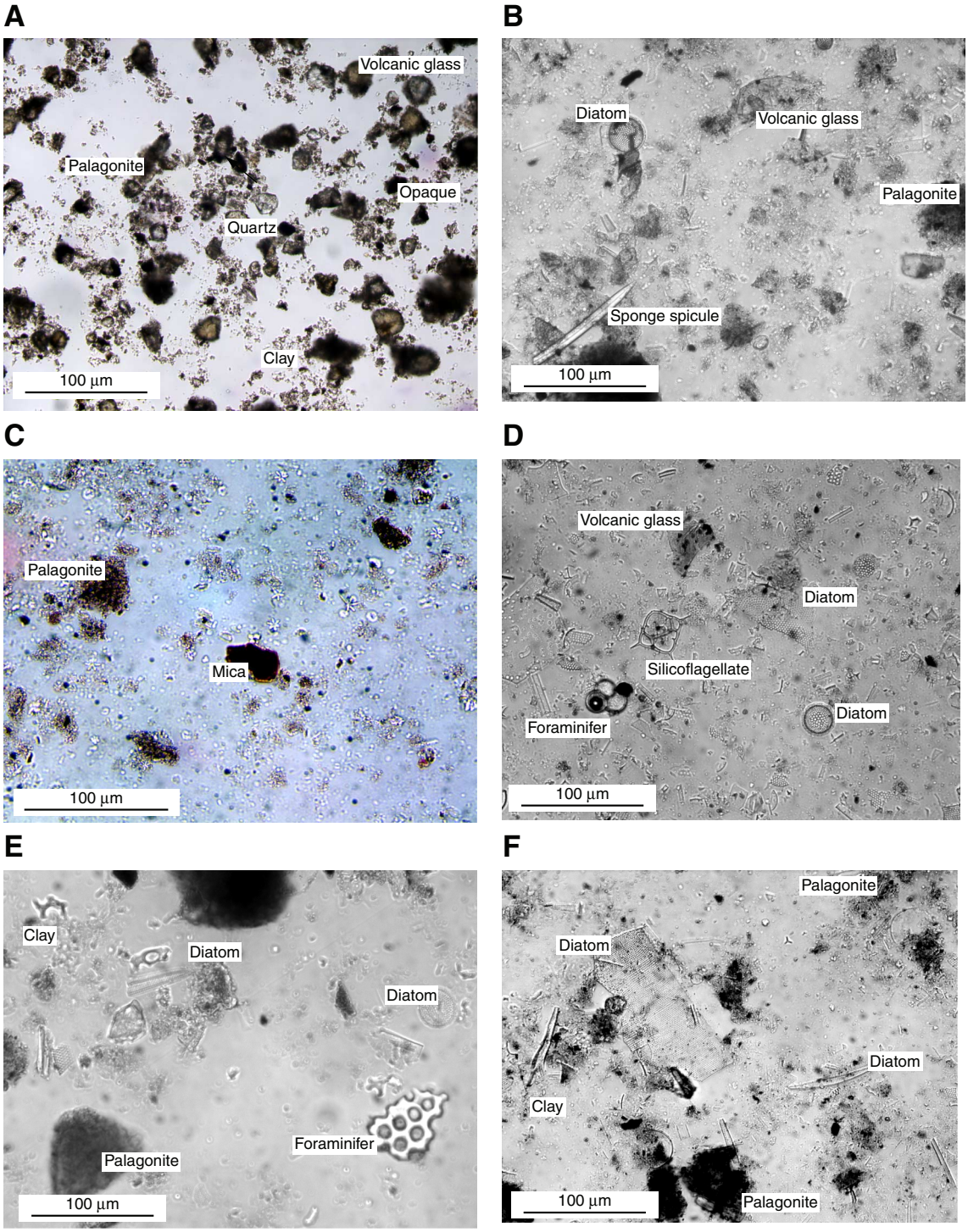

Figure F9. Close-up photograph showing the color contrast between the darker greenish gray claystone with silt in lithostratigraphic Unit T1 and the lighter, more clay rich diatom-bearing sediment in lithostratigraphic Subunit U1A (interval 205-1255A-3R-2, 8–25 cm).

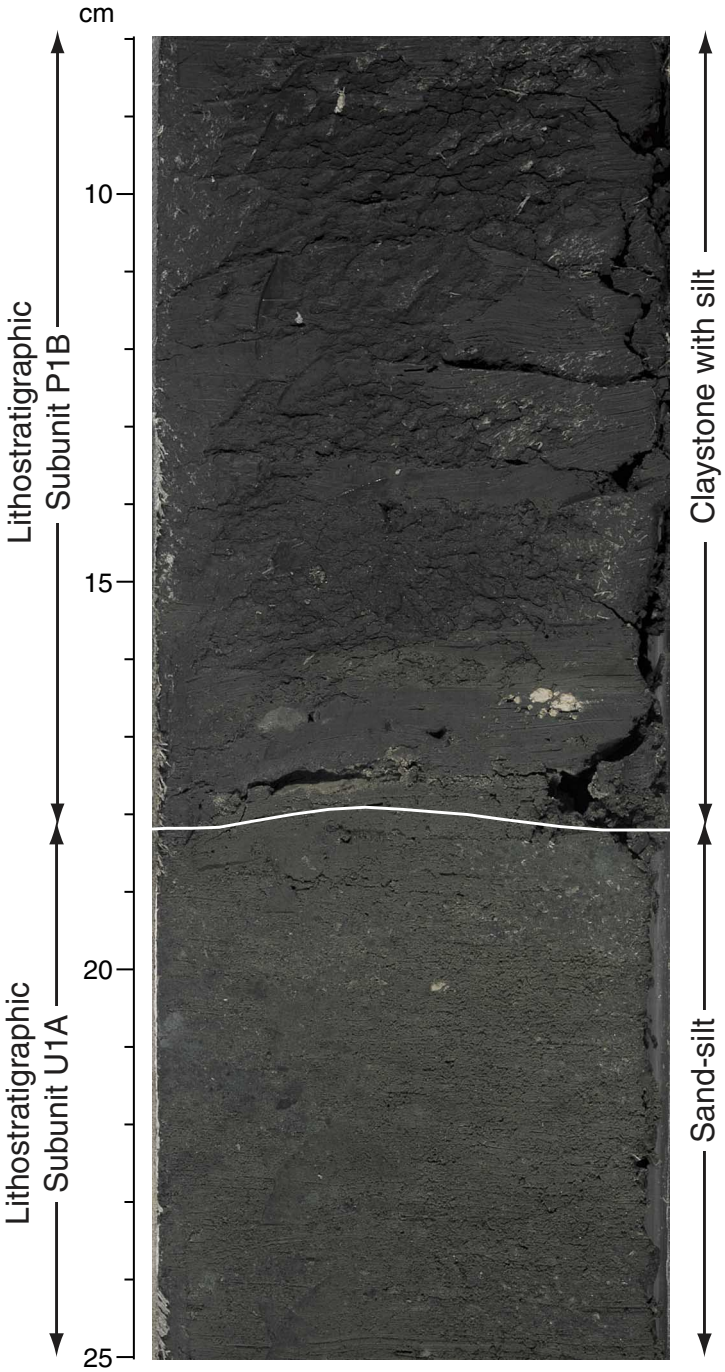

Figure F10. Close-up photograph showing a redeposited conglomeratic layer, which is interpreted as a trench turbidite deposit and part of lithostratigraphic Subunit U1A (interval 205-1255A-3R-3, 92–103 cm).

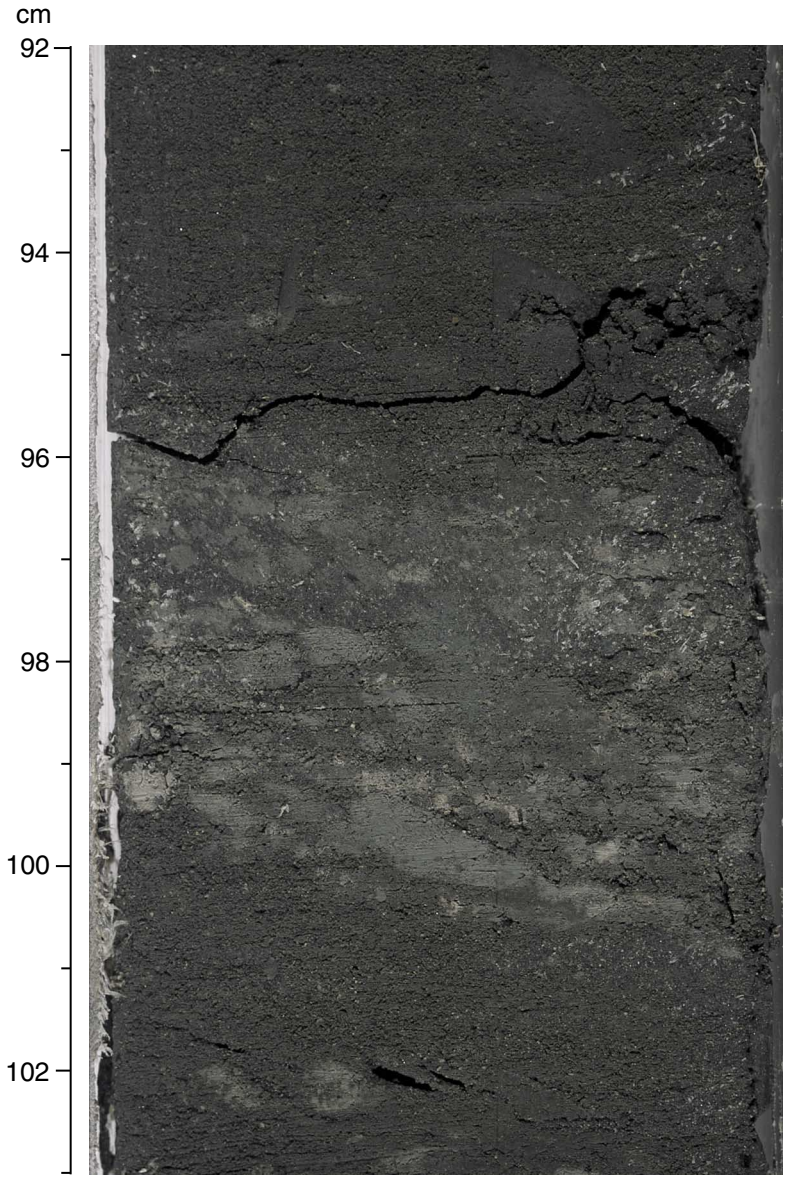

Figure F11. A. Close-up photograph showing a light-colored cobble of lithified limestone, which is interpreted as a block redeposited into the lower trench slope after sedimentation and lithification upslope (interval 205-1255A-3R-1, 142–150 cm). **B.** Smear slide photomicrograph of the cobble reveals a highly recrystallized matrix dominated by needles of calcite, with a minority component of more coherent carbonate grains.

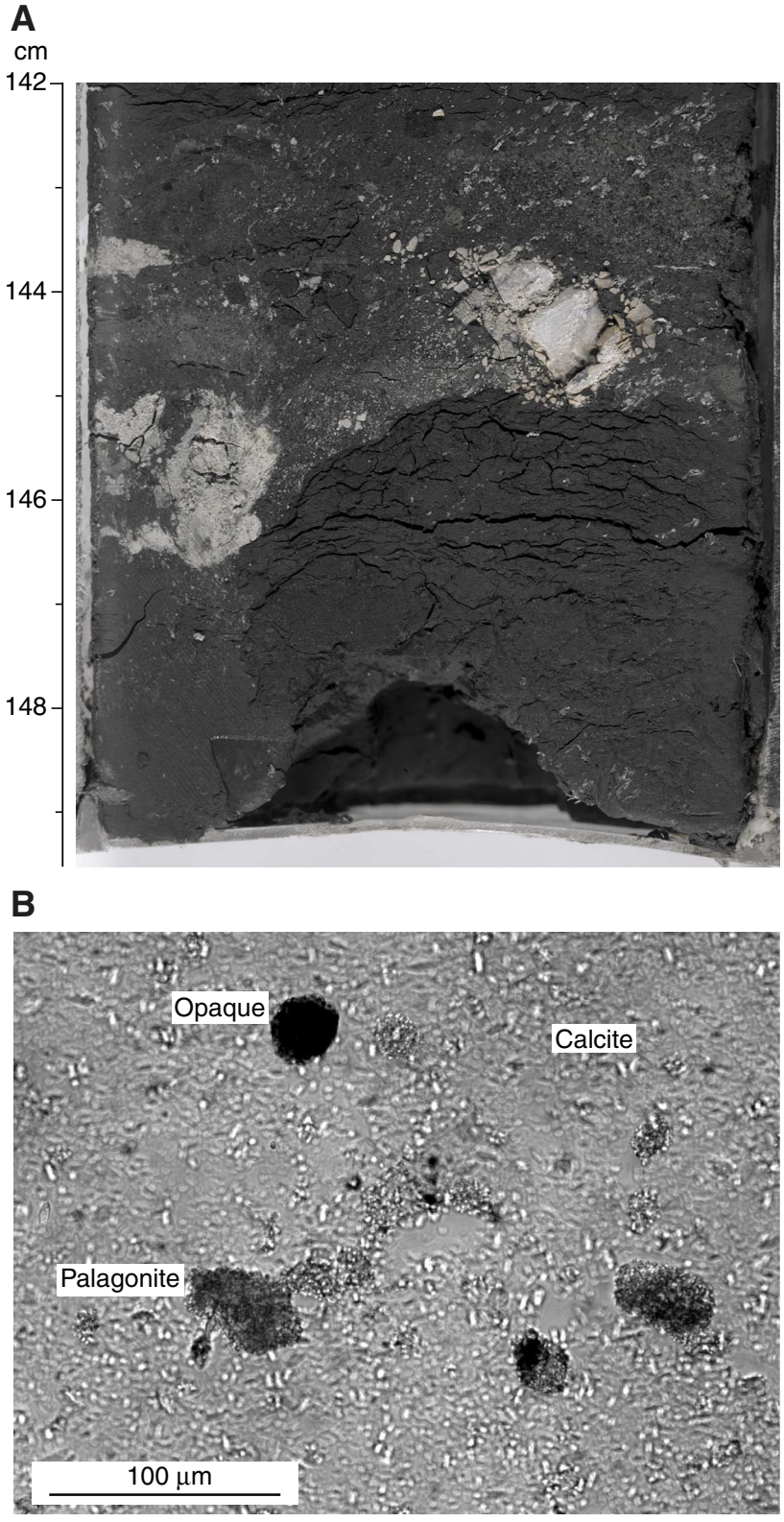

Figure F12. Close-up photograph showing the lithologic variation immediately below the lithostratigraphic boundary between Unit T1 and Subunit U1A (interval 205-1255A-3R-2, 35–50 cm). Note the well-bedded nannofossil chalk and underlying claystone that was slightly deformed during the coring process.

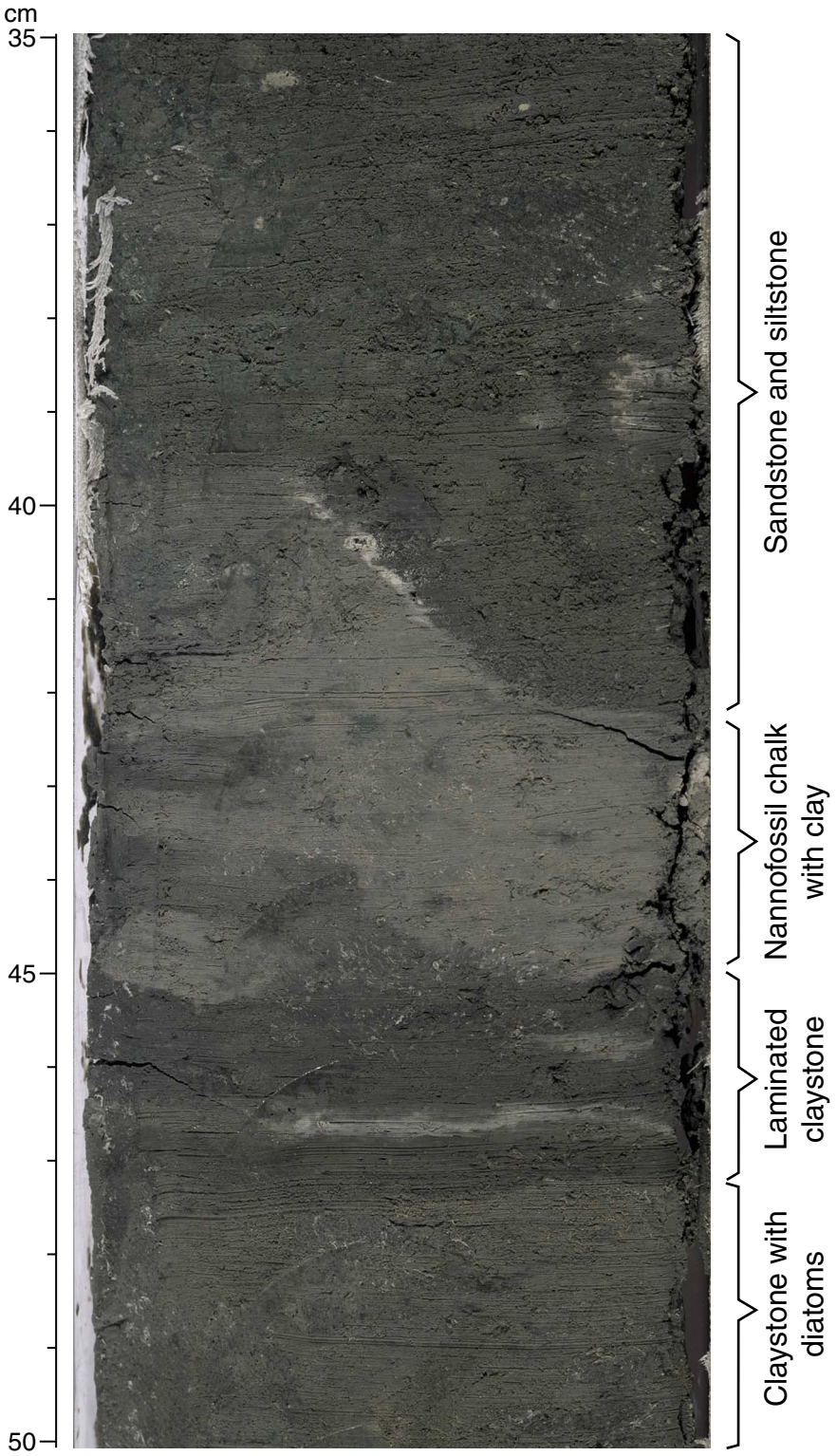

Figure F13. Close-up photograph showing the drilling-generated cobbles of lithified siltstone together with a small burrow infilled by a darker green silty material (interval 205-1255A-2R-1, 0–15 cm).

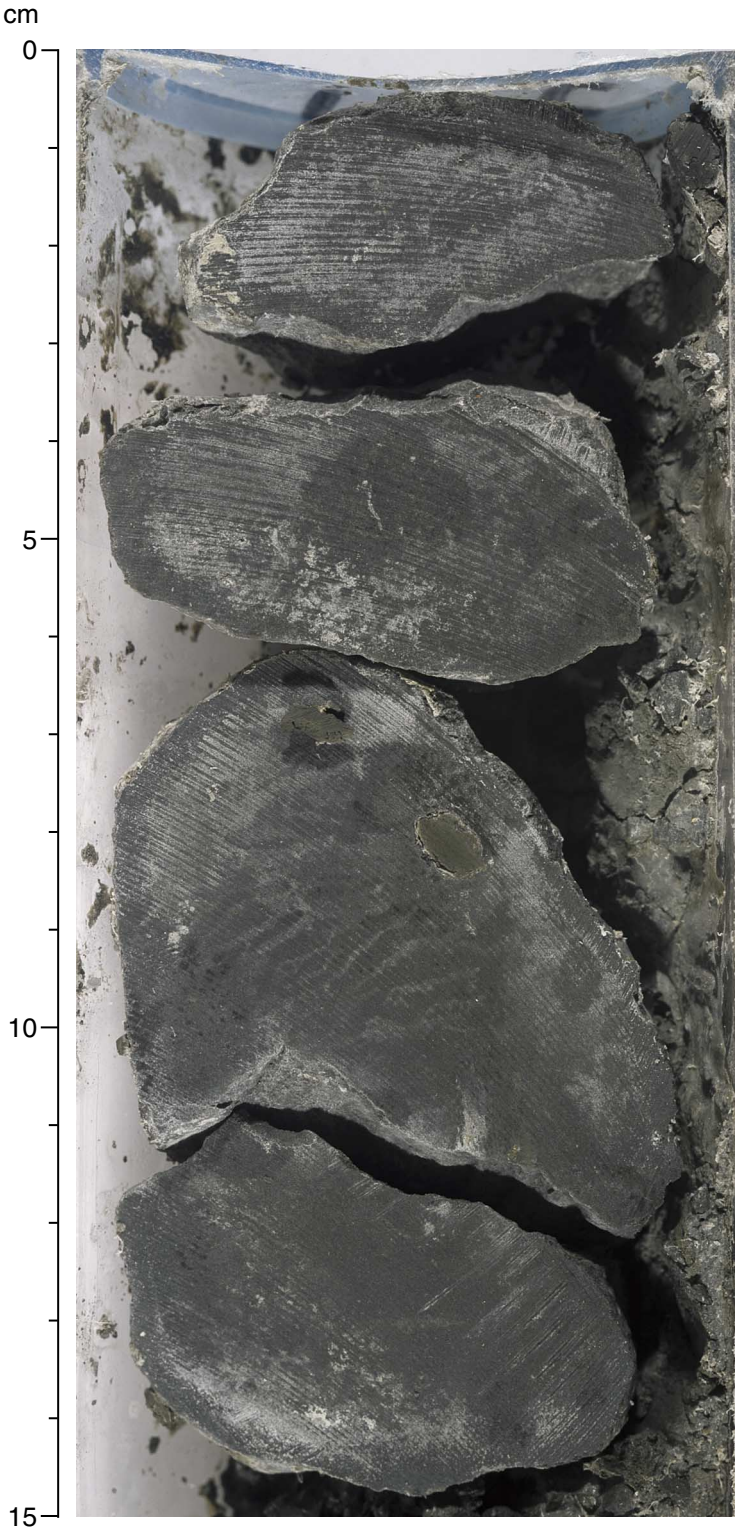

Figure F14. Structural and lithologic summary across the décollement zone. The density of fracturing is shown by the size of the brecciated fragments. Note the coincidence of lithologic and structural boundaries and the sharp decrease in deformation intensity across the base of the décollement.

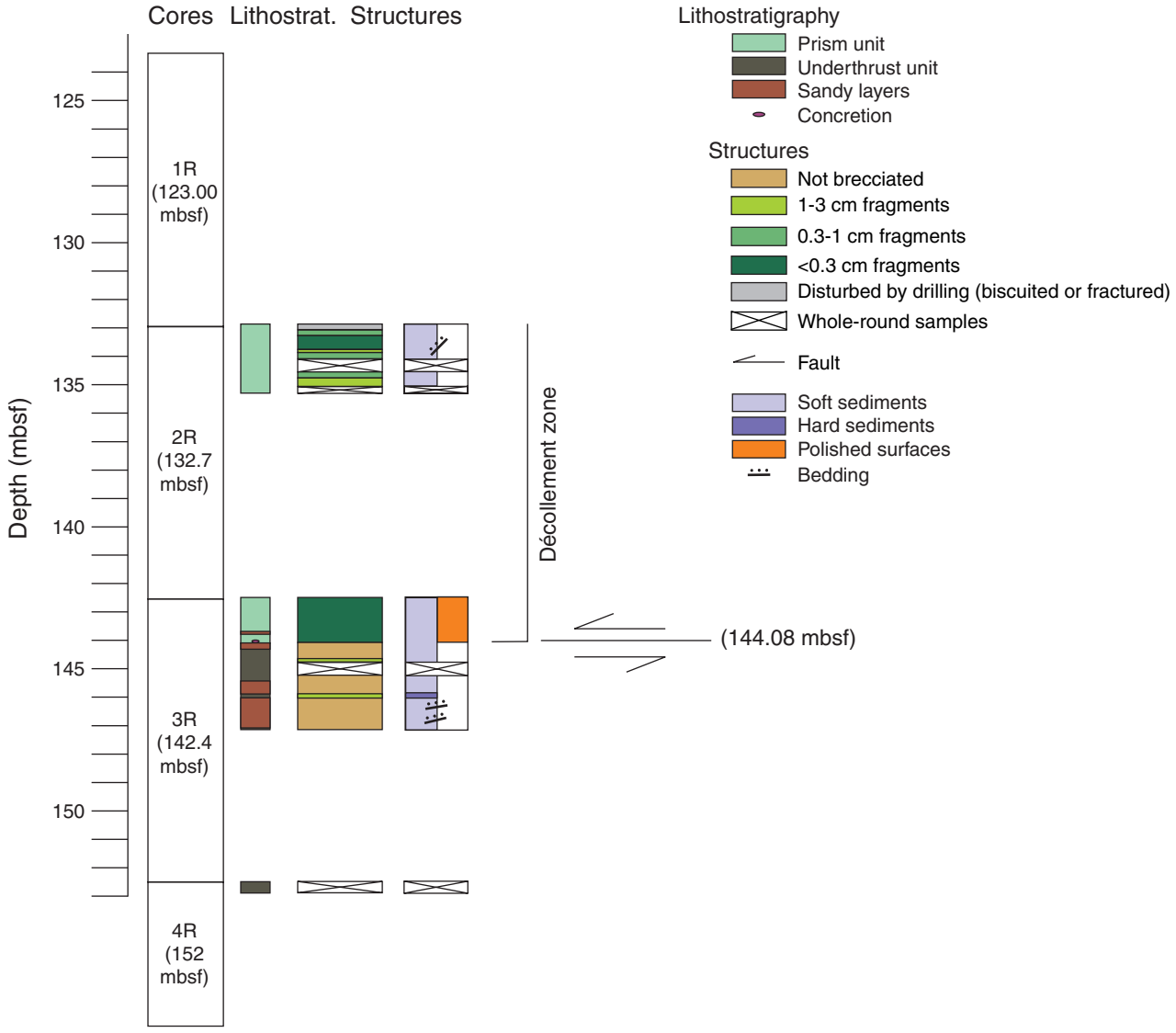

Figure F15. Close-up photograph of the base of the décollement zone and lithologic boundary between prism Unit T1 and hemipelagic Subunit U1A at 144.08 mbsf (interval 205-1255A-3R-2, 8–26 cm).

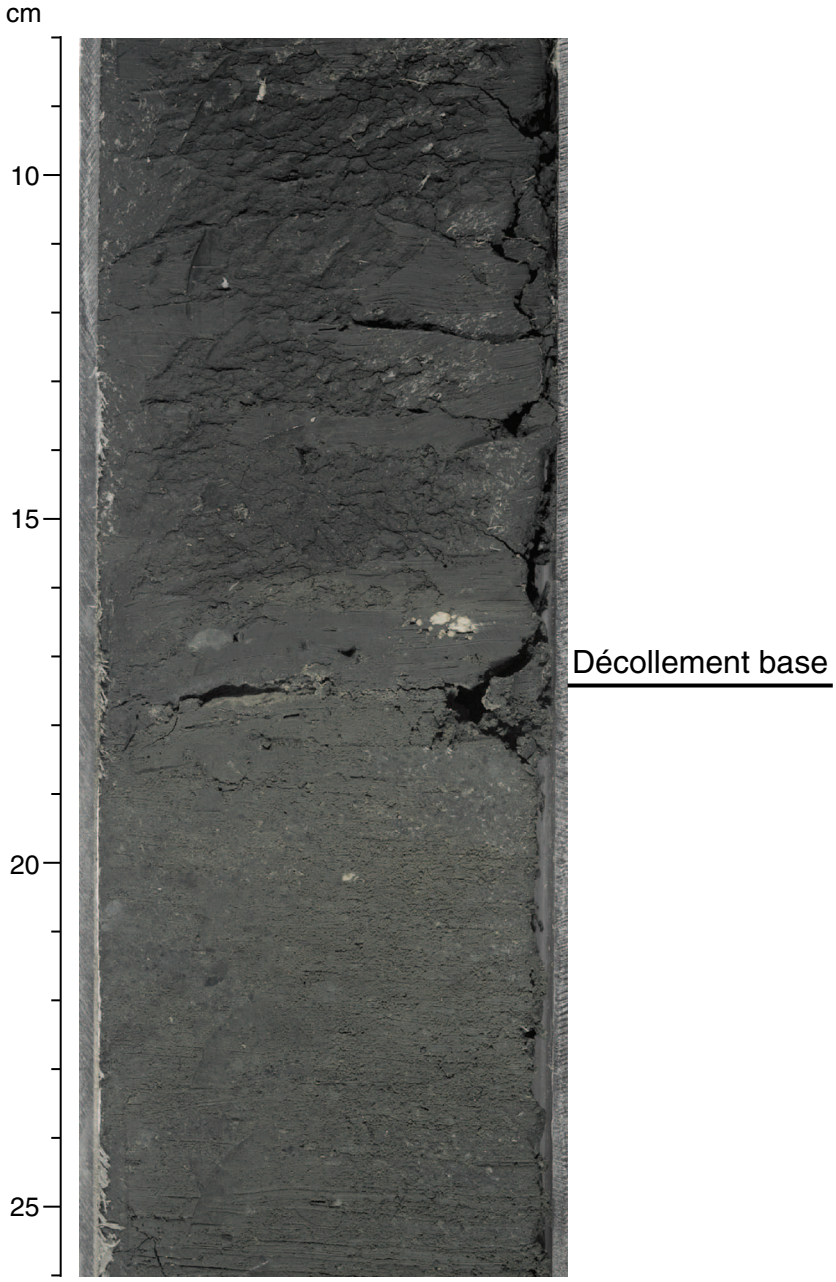

Figure F16. **A.** Porosity calculated from wet and dry mass and volume measurements. **B.** Bulk density. **C.** Corrected gamma ray attenuation (GRA) and moisture and density (MAD) bulk densities. The dashed line in all plots = the lower boundary of the décollement (144.08 mbsf).

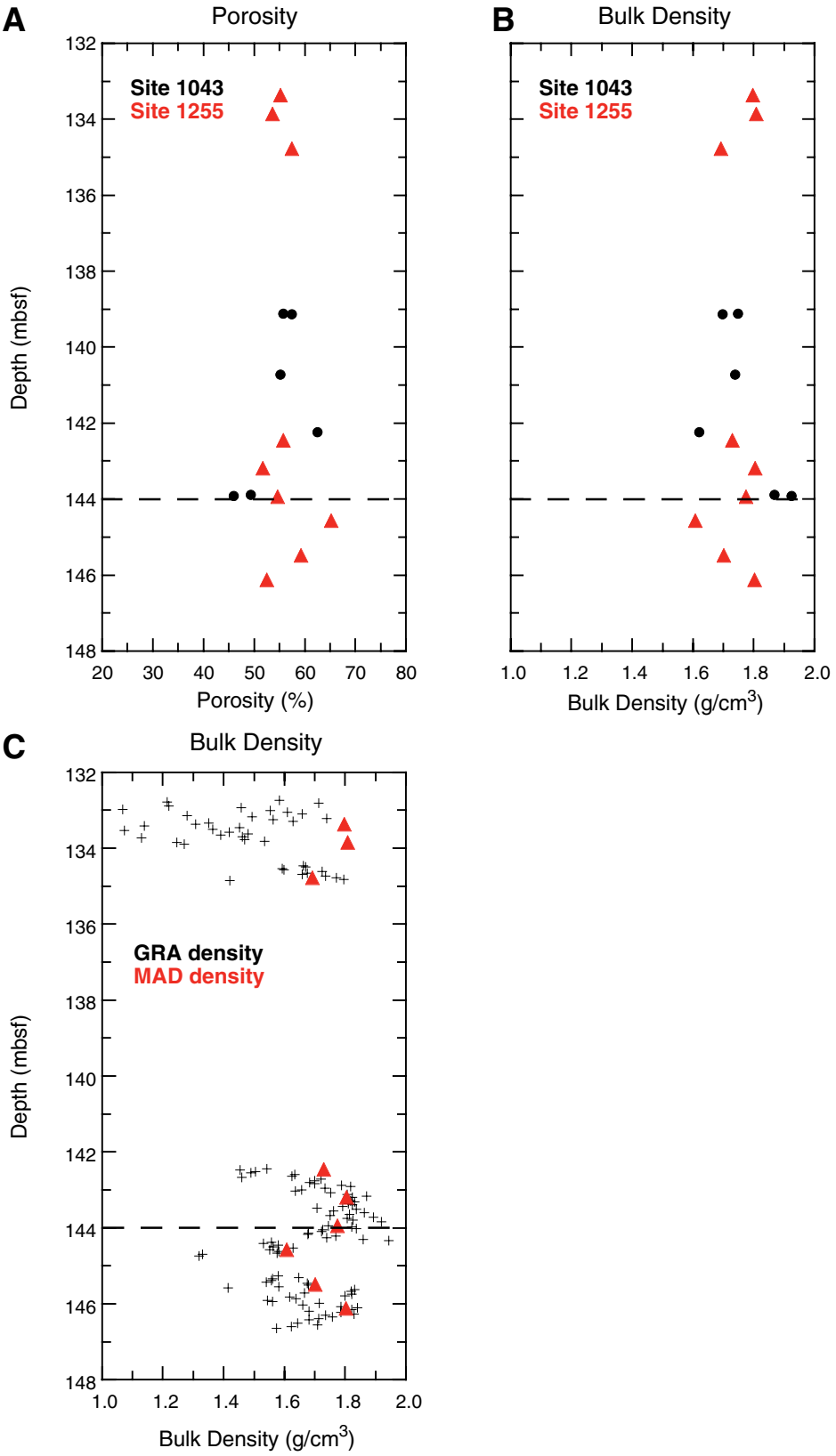

Figure F17. Grain densities determined from dry mass and volume measurements. The dashed line = the lower boundary of the décollement (144.08 mbsf).

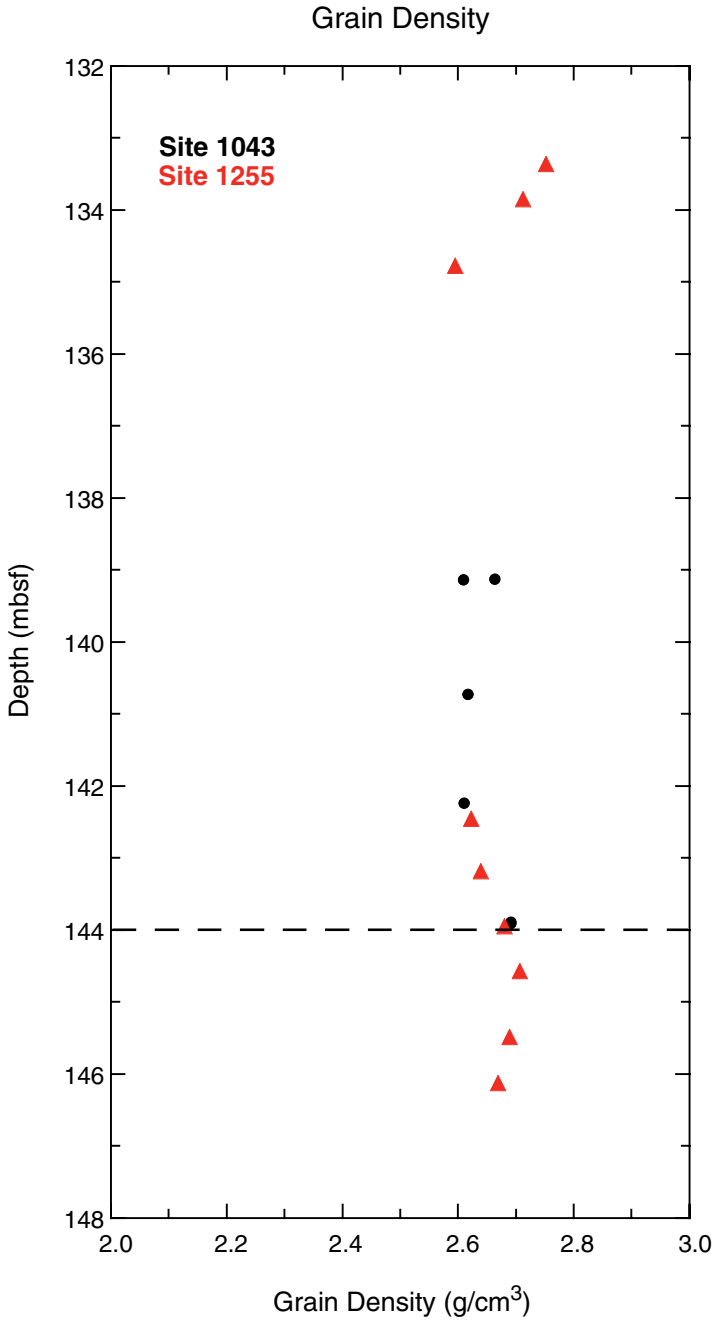

Figure F18. Uncorrected MST natural gamma ray (NGR) measurements. The dashed line = the lower boundary of the décollement (144.08 mbsf).

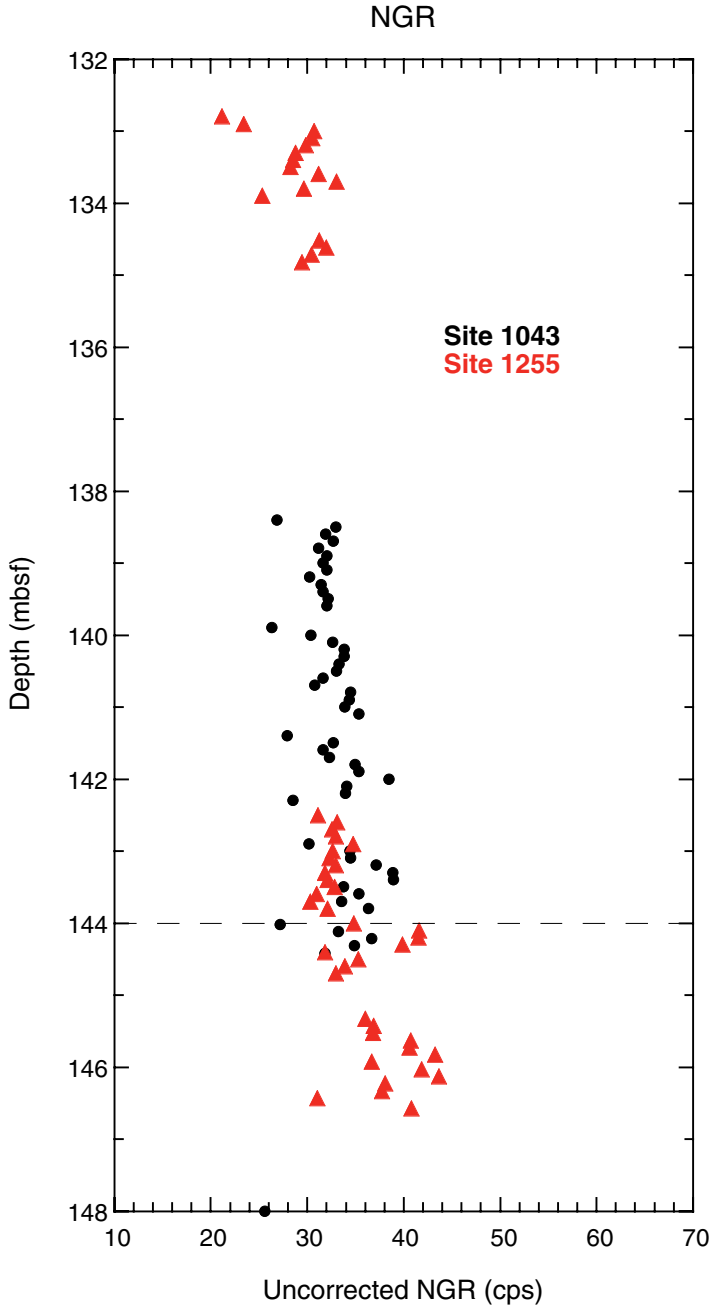

Figure F19. MST volumetric magnetic susceptibility (dimensionless). The dashed line = the lower boundary of the décollement (144.08 mbsf).

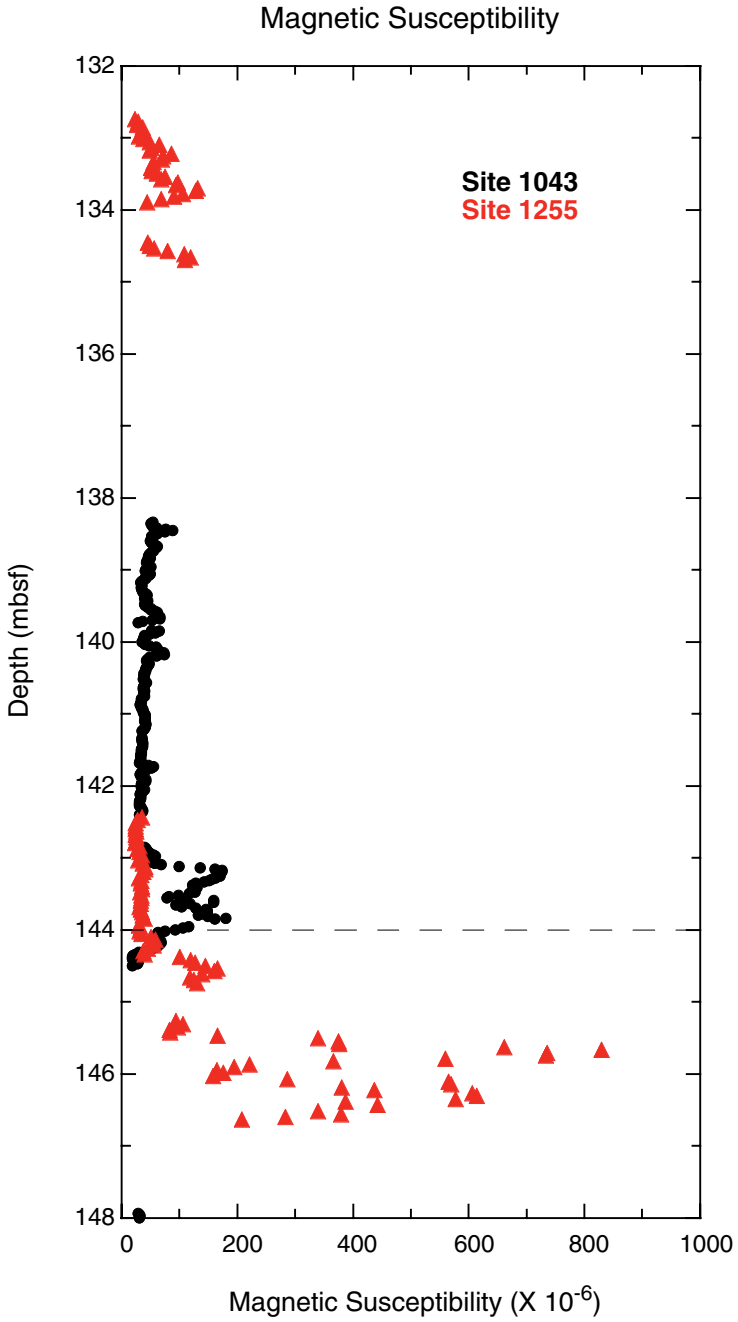

Figure F20. Magnetic polarity identification using declination and inclination changes of archive-half cores after 40-mT demagnetization with paleomagnetic data of discrete samples. Gray zone in polarity column = inconclusive polarity identification.

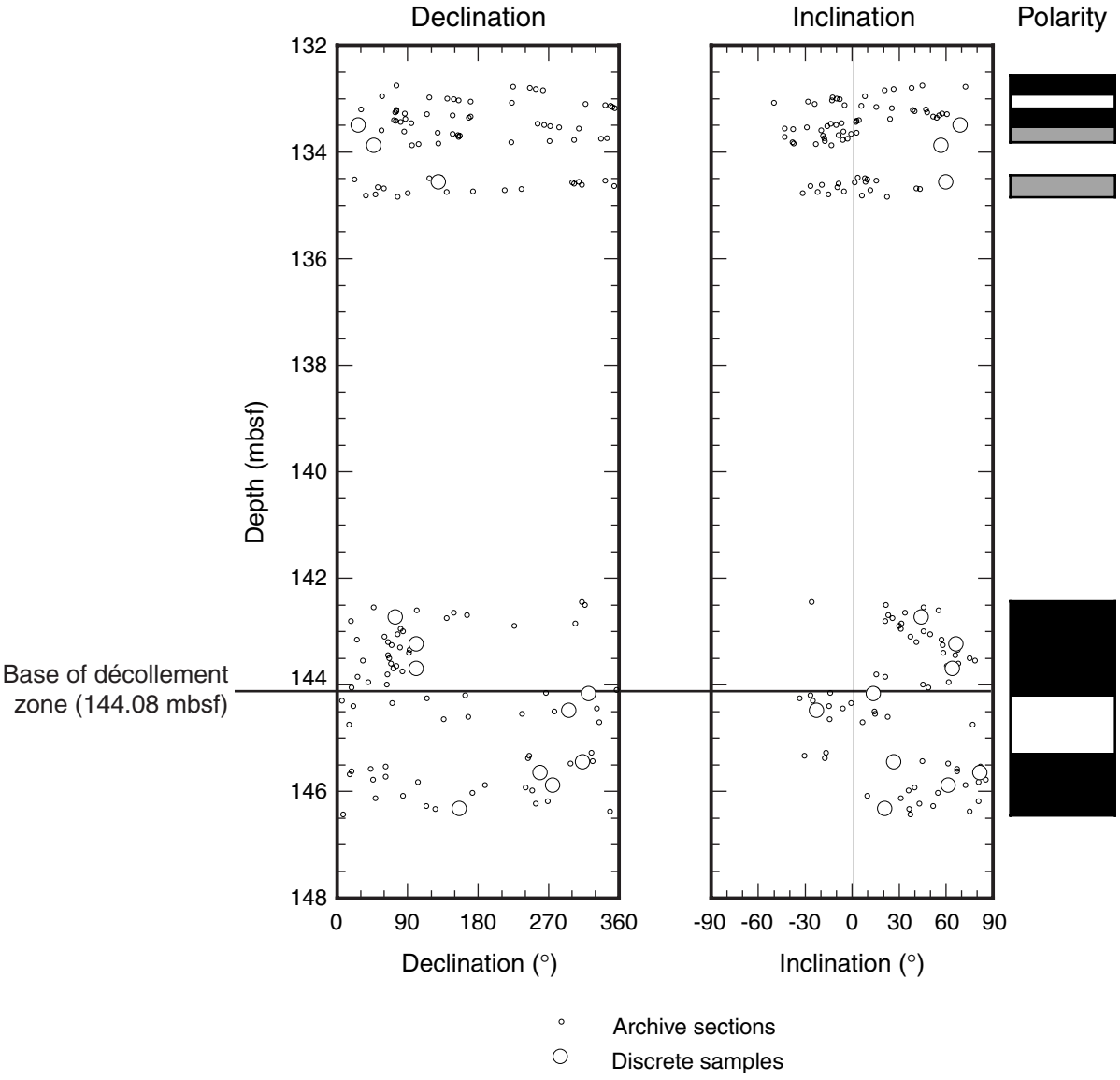

Figure F21. Natural remanent magnetization (NRM) intensity and magnetic susceptibility of archive-half cores. Archive multisensor track (AMST) data show susceptibility in the archive cores, and whole-round cores were measured using the multisensor track (MST).

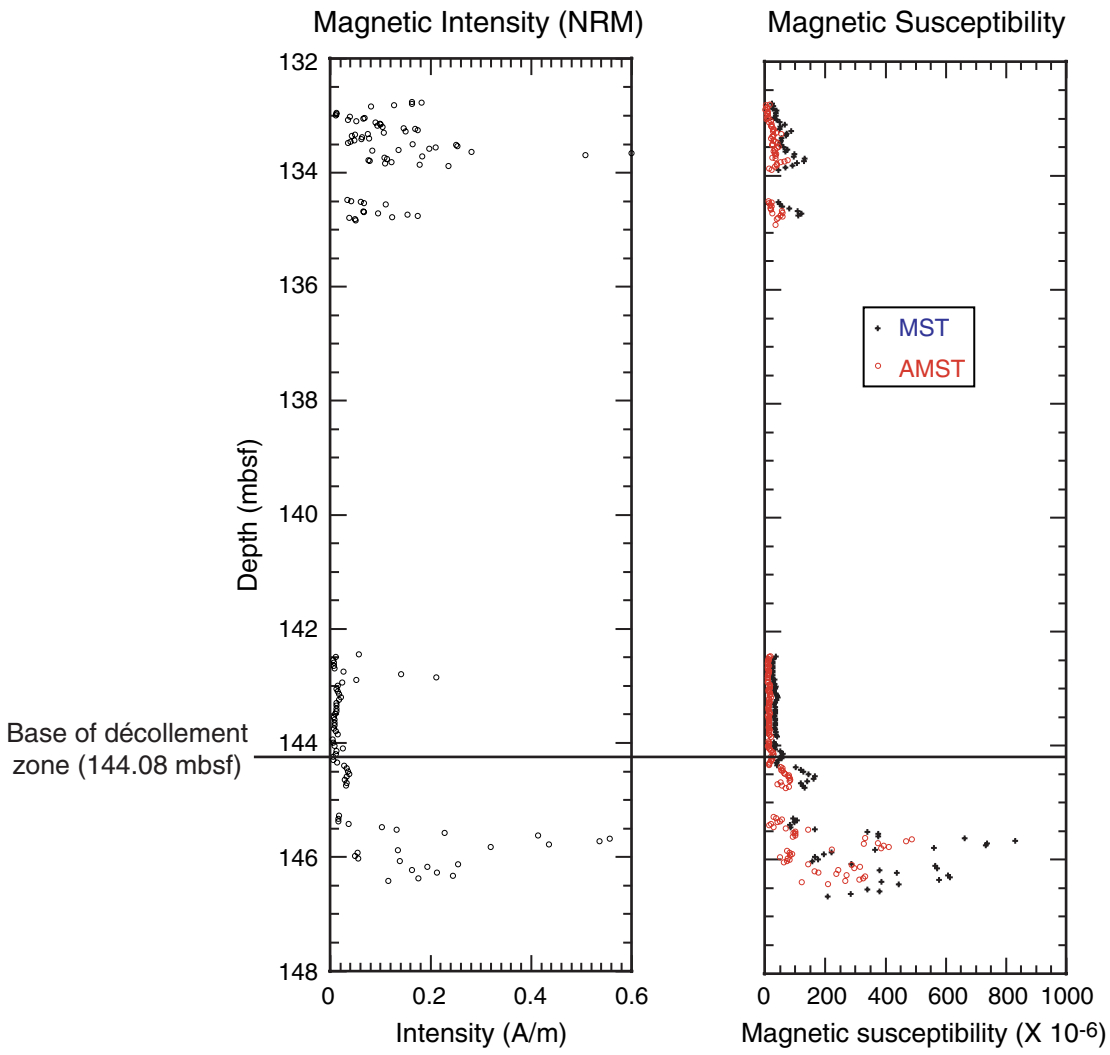

Figure F22. Results of headspace gas analyses for methane, ethane, and propane. The lithologic boundary as determined in "Structural Geology," p. 11, is at 144.08 mbsf.

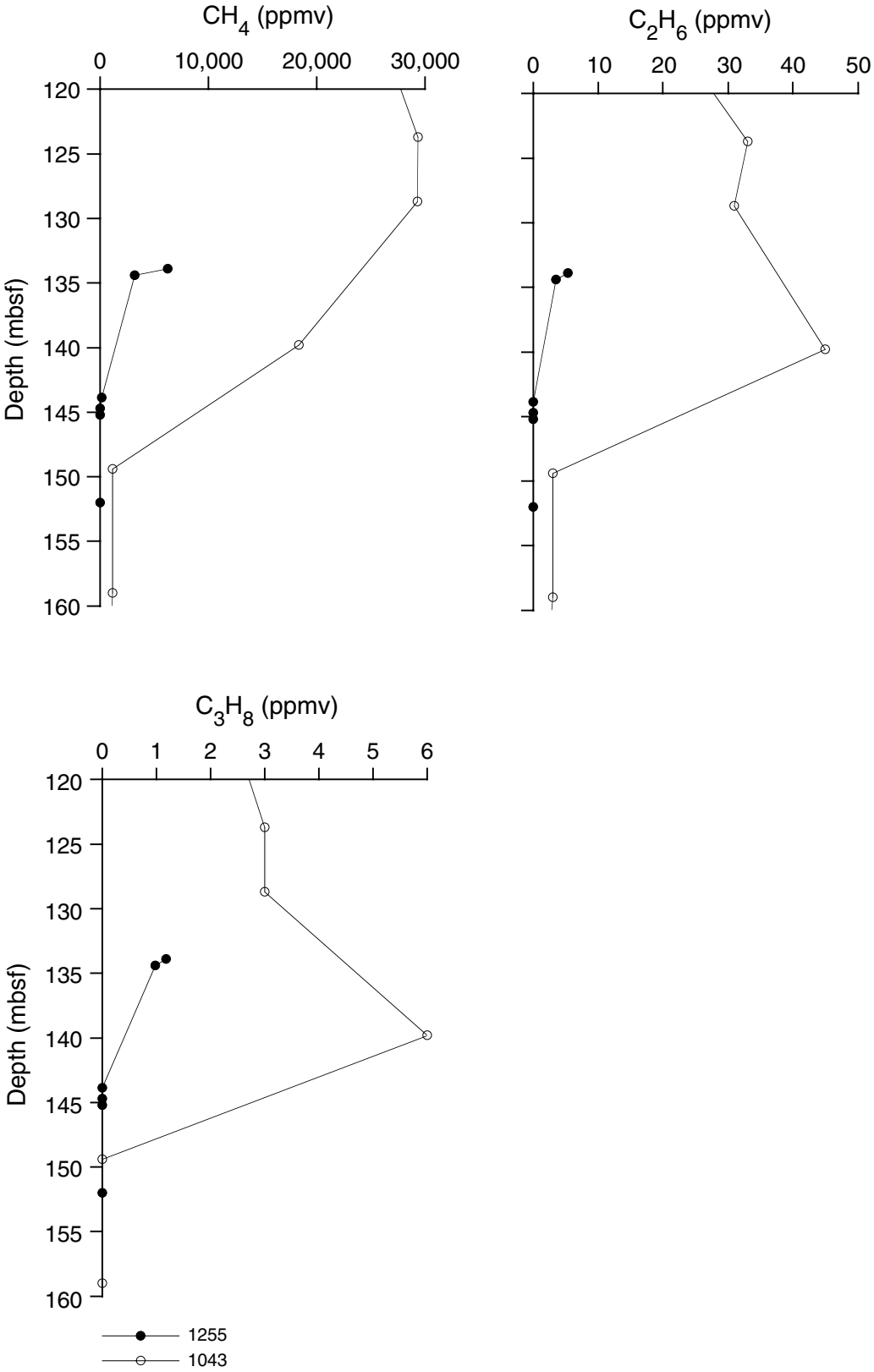

Table T1. Coring summary, Site 1255.

Hole 1255A
Latitude: 9°39.2716′N
Longitude: 86°11.1492′W
Time on site (hr): 167.25 (1645 hr, 26 Oct–1600 hr, 2 Nov 2002)
Seafloor (drill pipe measurement from rig floor, mbrf): 4323.0
Distance between rig floor and sea level (m): 11.4
Water depth (drill pipe measurement from sea level, m): 4311.6
Total depth (drill pipe measurement from rig floor, mbrf): 4480.0
Total penetration (meters below seafloor, mbsf): 157.0
Total length of cored section (m): 34.0
Total length of drilled intervals (m): 123.0
Total core recovered (m): 7.22
Core recovery (%): 21
Total number of cores: 4
Total number of drilled intervals: 1

Core	Date (Oct 2002)	Ship local time* (hr)	Depth (mbsf) Top	Depth (mbsf) Bottom	Length (m) Cored	Length (m) Recovered	Recovery (%)	Remarks
205-1255A-								
			*****Drilled from 0.0 to 123.0 mbsf*****					AHC
1R	30	2245	123.0	132.7	9.7	0.00	0.0	AHC for 1 hr; no recovery
2R	31	0220	132.7	142.4	9.7	2.38	24.5	AHC; Whirl-Pak
3R	31	0555	142.4	152.0	9.6	4.29	44.7	AHC; Whirl-Pak; drilling break at 147 mbsf
4R	31	0755	152.0	157.0	5.0	0.55	11.0	AHC; Whirl-Pak
				Cored totals:	34.0	7.22	21.2	
				Drilled total:	123.0			
				Total:	157.0			

Note: * = Ship local time is Universal Time Coordinated – 5 hr. AHC = active heave compensation. Whirl-Pak = microbiology microsphere contamination testing.

Table T2. Bulk geochemical analysis of sediments, Hole 1255A.

Core, section, interval (cm)	Depth (mbsf)	Major element oxide (wt%)												Trace element (ppm)					
		SiO_2	TiO_2	Al_2O_3	Fe_2O_3	MnO	CaO	MgO	Na_2O	K_2O	P_2O_5	Ti/Al	Total	Ba	Cr	Sr	V	Y	Zr
205-1255A-																			
2R-2, 0–43	133.94	51.14	1.06	16.09	8.60	0.06	3.86	3.32	2.30	1.84	0.15	0.07	88.42	393	106	278	175.1	17.5	97.9
3R-2, 87–127	144.77	53.65	0.85	15.11	7.86	0.14	3.14	3.17	2.35	1.77	0.11	0.06	88.15	564	75	200	190.5	18.9	101.1
4R-1, 0–38	152.00	52.51	0.87	15.27	8.26	0.10	2.89	3.00	2.27	1.75	0.12	0.06	87.04	1248	84	205	180.7	18.2	99.0

Table T3. Peak intensities and peak areas from X-ray diffraction analysis of bulk-powder sediment samples, Leg 170, Hole 1043A.

Core, section, interval (cm)	Unit	Depth (mbsf)	X-ray diffraction peak intensities (cps)						X-ray diffraction peak areas (total count)					
			Composite clay	Quartz (101)	Plagioclase (002)	Calcite (104)	Quartz (100)	Cristobalite (101)	Composite clay	Quartz (101)	Plagioclase (002)	Calcite (104)	Quartz (100)	Cristobalite (101)
170-1043A-														
1H-2, 140	T1	2.90	109	267	102	341	63	54	3,710	3,501	1,299	4,504	1,069	875
1H-4, 140	T1	5.90	102	343	146	28	76	106	3,880	4,538	1,681	341	1,190	1,379
2H-1, 140	T1	9.40	101	334	114	15	63	119	3,472	4,243	1,370	230	1,117	1,532
2H-4, 135	T1	13.85	113	408	134	84	87	50	3,987	5,345	1,437	1,101	1,629	653
3X-1, 120	T1	18.10	121	492	180	36	103	66	4,273	6,747	2,315	452	1,852	983
4X-3, 0	T1	27.40	101	434	380	173	93	65	3,453	5,548	4,260	2,247	1,555	812
5X-4, 52	T1	38.42	90	484	212	133	97	60	3,353	6,256	2,442	1,739	1,621	838
6X-3, 115	T1	46.95	96	456	180	70	94	61	3,473	6,001	2,218	859	1,523	922
7X-5, 65	T1	58.64	86	467	137	207	81	61	3,374	5,732	1,831	2,736	1,184	767
8X-3, 115	T1	65.75	125	481	151	36	122	65	4,029	6,837	1,818	419	1,970	963
9X-5, 115	T1	78.35	114	474	101	69	88	48	4,016	6,007	1,280	853	1,533	617
10X-2, 115	T1	83.35	108	397	222	75	79	52	3,621	5,589	2,469	1,073	1,496	764
11X-2, 115	T1	92.95	101	323	153	100	62	66	3,845	5,736	1,562	1,633	1,216	1,501
12X-4, 115	T1	105.55	103	402	203	130	93	66	3,865	5,333	2,207	2,347	1,429	892
13X-4, 90	T1	114.90	82	301	119	80	65	51	3,142	4,382	1,394	1,043	950	647
14X-4, 115	T1	124.85	82	377	116	61	69	65	2,672	4,755	1,594	883	1,036	879
15X-1, 96	T1	129.66	93	344	144	35	78	76	3,271	4,484	1,544	306	1,260	1,038
16X-3, 115	T1	142.45	96	483	147	72	109	55	3,300	5,834	1,603	891	1,506	788
17X-2, 115	U1B	150.55	100	473	147	46	90	69	3,521	5,829	1,640	636	1,375	1,064
18X-2, 115	U1B	160.15	81	237	117	119	52	60	3,060	3,265	1,290	1,652	834	794
19X-3, 95	U1B	171.05	83	280	66	98	69	61	3,291	3,727	957	1,150	1,101	772
20X-2, 130	U1B	179.40	71	251	62	91	54	51	2,914	3,250	748	1,327	921	725
21X-5, 130	U1B	193.30	89	282	64	185	65	42	3,179	3,731	814	2,384	928	679
23X-4, 130	U2A	211.00	82	288	116	24	62	100	2,745	3,703	1,188	264	943	1,270
24X-3, 125	U2A	219.05	124	377	88	41	67	377	4,797	4,845	1,152	451	1,234	4,845
26X-4, 125	U2A	239.85	99	307	128	66	58	59	3,805	4,191	1,355	769	839	821
27X-4, 125	U2B	249.45	105	255	80	109	65	60	3,999	3,789	854	1,405	1,099	945
28X-4, 125	U2B	259.05	80	183	68	429	40	56	3,271	2,489	796	5,021	568	560
29X-3, 125	U3A	267.25	39	54	77	1,317	21	45	1,492	749	873	15,501	305	541
30X-1, 120	U3A	273.80	28	32	18	2,068	13	18	841	321	204	26,431	148	257

Note: cps = count per second. The numbers in parentheses are Miller indexes.

Table T4. Peak area ratios of dominant minerals, Leg 170, Hole 1043A.

Core, section, interval (cm)	Unit/ subunit	Depth (mbsf)	Peak areas relative to quartz (101)			Peak area ratio
			Clay/ Quartz	Plagioclase/ Quartz	Calcite/ Quartz	Cristobalite (101)/ Quartz (100)
170-1043A-						
1H-2, 140	T1	2.90	1.06	0.37	1.29	0.82
1H-4, 140	T1	5.90	0.86	0.37	0.08	1.16
2H-1, 140	T1	9.40	0.82	0.32	0.05	1.37
2H-4, 135	T1	13.85	0.75	0.27	0.21	0.40
3X-1, 120	T1	18.10	0.63	0.34	0.07	0.53
4X-3, 0	T1	27.40	0.62	0.77	0.41	0.52
5X-4, 52	T1	38.42	0.54	0.39	0.28	0.52
6X-3, 115	T1	46.95	0.58	0.37	0.14	0.61
7X-5, 65	T1	58.64	0.59	0.32	0.48	0.65
8X-3, 115	T1	65.75	0.59	0.27	0.06	0.49
9X-5, 115	T1	78.35	0.67	0.21	0.14	0.40
10X-2, 115	T1	83.35	0.65	0.44	0.19	0.51
11X-2, 115	T1	92.95	0.67	0.27	0.28	1.23
12X-4, 115	T1	105.55	0.72	0.41	0.44	0.62
13X-4, 90	T1	114.90	0.72	0.32	0.24	0.68
14X-4, 115	T1	124.85	0.56	0.34	0.19	0.85
15X-1, 96	T1	129.66	0.73	0.34	0.07	0.82
16X-3, 115	T1	142.45	0.57	0.27	0.15	0.52
17X-2, 115	U1B	150.55	0.60	0.28	0.11	0.77
18X-2, 115	U1B	160.15	0.94	0.40	0.51	0.95
19X-3, 95	U1B	171.05	0.88	0.26	0.31	0.70
20X-2, 130	U1B	179.40	0.90	0.23	0.41	0.79
21X-5, 130	U1B	193.30	0.85	0.22	0.64	0.73
23X-4, 130	U2A	211.00	0.74	0.32	0.07	1.35
24X-3, 125	U2A	219.05	0.99	0.24	0.09	3.93
26X-4, 125	U2A	239.85	0.91	0.32	0.18	0.98
27X-4, 125	U2B	249.45	1.06	0.23	0.37	0.86
28X-4, 125	U2B	259.05	1.31	0.32	2.02	0.99
29X-3, 125	U3A	267.25	1.99	1.17	20.70	1.77
30X-1, 120	U3A	273.80	2.62	0.64	82.34	1.74

Note: Numbers in parentheses are Miller indexes.

Table T5. Peak intensities and peak areas from X-ray diffraction analysis of bulk-powder sediment samples, Leg 205, Hole 1255A.

Core, section, interval (cm)	Unit	Depth (mbsf)	X-ray diffraction peak intensities (cps)						X-ray diffraction peak areas (total count)					
			Composite clay	Quartz (101)	Plagioclase (002)	Calcite (104)	Quartz (100)	Cristobalite (101)	Composite clay	Quartz (101)	Plagioclase (002)	Calcite (104)	Quartz (100)	Cristobalite (101)
205-1255A-														
2R-1, 105–106	T1	133.75	85	713	363	127	133	72	3,024	8,747	4,571	1,605	1,998	1,146
2R-2, 0–43	T1	133.94	102	514	1,178	114	114	72	3,526	6,630	10,931	1,620	1,616	925
2R-3, 45–46	T1	134.87	74	445	240	317	89	65	2,875	5,970	2,903	4,495	1,374	864
3R-1, 127–128	T1	143.67	127	476	178	153	98	66	4,491	6,719	2,162	2,309	1,532	911
3R-2, 87–127	T1	144.77	106	335	125	92	78	64	4,009	4,638	1,808	1,386	1,147	1,005
3R-3, 61–62	T1	145.84	81	290	214	79	68	86	2,865	4,129	2,664	1,053	1,043	1,165
4R-1, 0–38	T1	152.00	108	348	160	54	81	112	3,965	5,071	2,076	687	1,393	1,525

Notes: cps = count per second. Numbers in parentheses are Miller indexes.

Table T6. Peak area ratios of dominant minerals, Hole 1255A.

Core, section, interval (cm)	Unit	Depth (mbsf)	Peak areas relative to quartz (101)			Peak area ratio
			Clay/ Quartz	Plagioclase/ Quartz	Calcite/ Quartz	Cristobalite (101)/ Quartz (100)
205-1255A-						
2R-1, 105–106	T1	133.75	0.35	0.52	0.18	0.57
2R-2, 0–43	T1	133.94	0.53	1.65	0.24	0.57
2R-3, 45–46	T1	134.87	0.48	0.49	0.75	0.63
3R-1, 127–128	T1	143.67	0.67	0.32	0.34	0.59
3R-2, 87–127	T1	144.77	0.86	0.39	0.30	0.88
3R-3, 61–62	T1	145.84	0.69	0.65	0.26	1.12
4R-1, 0–38	T1	152.00	0.78	0.41	0.14	1.09

Note: Numbers in parentheses are Miller indexes.

Table T7. Pore water chemical data of major constituents, Hole 1255A.

Core, section, interval (cm)	Depth (mbsf)	Volume (cm^3)	pH	Alkalinity (mM)	Salinity	Cl (mM)	SO_4 (mM)	Na* (mM)	Mg (mM)	K (mM)	Ca (mM)	Mg/Ca	Na/Cl
205-1255A-													
2R-2, 0–43	134.2	14	ND	ND	32	549	0.00	452.34	38.08	11.18	4.66	8.17	0.82
3R-2, 87–127	145.0	46	8.01	22.65	33	559	7.25	479.42	46.05	13.42	5.60	8.22	0.86
4R-1, 0–38	152.2	41	7.75	18.42	34	557	8.61	472.81	45.09	12.74	8.45	5.33	0.85

Notes: * = alkalinity not included in charge balance. ND = not determined.

Table T8. Pore water chemical data of minor constituents, Hole 1255A.

Core, section, interval (cm)	Depth (mbsf)	Volume (cm^3)	B (μM)	Ba (μM)	Fe (μM)	Li (μM)	Mn (μM)	Sr (μM)	Si (μM)	NH_4 (μM)
205-1255A-										
2R-2, 0–43	134.2	14	352.90	9.29	4.57	32.89	2.97	98.42	623.90	2943.10
3R-2, 87–127	145.8	46	511.56	4.04	8.34	30.91	5.80	94.76	695.90	1843.10
4R-1, 0–38	152.2	41	624.67	3.15	3.34	26.69	26.08	96.74	717.90	643.10

Table T9. Composition of headspace gases, Hole 1255A.

Core, section, interval (cm)	Depth (mbsf)	CH_4 (ppmv)	C_2H_6 (ppmv)	C_2H_4 (ppmv)	C_3H_8 (ppmv)	CH_4/C_2H_6	*i*-C_4H_{10} (ppmv)	*n*-C_4H_{10} (ppmv)	*i*-C_5H_{12} (ppmv)	*n*-C_5H_{12} (ppmv)	O_2 (ppmv)	N_2 (ppmv)	CO_2 (ppmv)
205-1255A-													
2R-1, 119–124	133.89	6,259	5	0	1	1163	0	0	0	0	134,744	667,696	15,483
2R-3, 0–5	134.42	3,231	4	0	1	923	0	0	0	0	144,156	759,393	5,246
3R-1, 145–150	143.85	176	0	1	0	ND	0	0	0	0	152,929	722,062	11,794
3R-2, 82–87	144.72	6	0	0	0	ND	0	0	0	0	106,983	770,170	6,195
3R-3, 0–5	145.23	4	0	0	0	ND	0	0	0	0	117,785	771,614	8,274
4R-1, 0–5	152.00	7	0	1	0	ND	0	0	0	0	144,635	719,433	7,332

Notes: ppmv = parts per million by volume. ND = not determined.

Table T10. Composition of vacutainer gases, Hole 1255A.

Core, section, interval (cm)	Depth (mbsf)	CH_4 (ppmv)	C_2H_6 (ppmv)	C_3H_8 (ppmv)	CH_4/C_2H_6	*i*-C_4H_{10} (ppmv)	*n*-C_4H_{10} (ppmv)	*i*-C_5H_{12} (ppmv)	*n*-C_5H_{12} (ppmv)	O_2 (ppmv)	N_2 (ppmv)	CO_2 (ppmv)
205-1255A-												
2R-1, 123–124	133.93	194	0	0	ND	0	0	0	0	189,865	764,241	147
3R-1, 91–92	143.31	93	0	0	ND	0	0	0	0	189,636	765,959	267
3R-2, 18–19	144.08	ND	ND	ND	ND	ND	ND	ND	ND	ND	ND	ND
3R-3, 82–83	146.05	860	1	1	722	0	0	0	0	180,028	773,737	208

Notes: ppmv = parts per million by volume. ND = not determined.

Table T11. Calcium carbonate, inorganic carbon, total carbon, total nitrogen, total sulfur, and total organic carbon contents in sediments, Hole 1255A.

Core, section, interval (cm)	Depth (mbsf)	$CaCO_3$ (wt%)	IC (wt%)	TC (wt%)	TN (wt%)	TS (wt%)	TOC (wt%)	TOC/TN
205-1255A-								
2R-2, 0–43	133.94	4.77	0.57	1.73	0.17	0.41	1.16	6.9
3R-2, 87–127	144.77	2.66	0.32	1.28	0.16	0.40	0.96	6.1
4R-1, 0–38	152.00	1.64	0.20	1.88	0.21	1.01	1.68	7.9

Notes: IC = inorganic carbon, TC = total carbon, TN = total nitrogen, TS = total sulfur, TOC = total organic carbon. Accuracies of TS and TN are low, ~20% (see "Organic Geochemistry," p. 26, in the "Explanatory Notes" chapter).

Table T12. Rock-Eval data, Hole 1255A.

Core, section, interval (cm)	Depth (mbsf)	T_{max} (°C)	S_1 (mg HC/g)	S_2 (mg HC/g)	PI ($S_1/[S_1+S_2]$)	PC ($0.083 \times S_1/S_2$)	HI (mg HC/g TOC)	TOC (wt%)
205-1255A-								
2R-2, 0–43	133.94	394	0.46	1.65	0.22	0.023	142	1.16
3R-2, 87–127	144.77	412	0.22	0.95	0.19	0.019	99	0.96
4R-1, 0–38	152.00	406	0.51	1.91	0.21	0.022	114	1.68

Notes: T_{max} = temperature of maximum hydrocarbon generation from kerogen. S_1 = volatile hydrocarbons, S_2 = kerogen-derived hydrocarbons. PI = productivity index. PC = pyrolizable carbon. HI = hydrogen index. TOC = total organic carbon obtained by CNS-elemental analysis.